GUISNET Louis

Master Nanotech per ICT
2019

ONERA - The French Aerospace Lab
Centre de Châtillon - 29, avenue de la Division Leclerc 92320 CHATILLON

Development of a MEMS magnetometer

from 04/03/19 to 02/08/19

Confidentiality: no

Under the supervision of:

- **Company supervisor : Thomas PERRIER, thomas.perrier@onera.fr**
- **Phelma Tutor : Liliana PREJBANU, liliana.buda@cea.fr**
- **Politecnico di Tirino Tutor: Carlo Ricciardi, carlo.ricciardi@polito.it**

Ecole nationale
supérieure de physique,
électronique, matériaux

Phelma
Bât. Grenoble INP - Minatec
3 Parvis Louis Néel - CS 50257
F-38016 Grenoble Cedex 01

Tél +33 (0)4 56 52 91 00
Fax +33 (0)4 56 52 91 03

http://phelma.grenoble-inp.fr

Acknowledgments

This master thesis internship took place in the Microsensor unit at the ONERA (Office national d'Etudes et de Recheches Aérospaciales) and I would like to thank all the people I had the opportunity to meet and to work with.
First of all I would like to thank Mr Raphael Levy in charge of the team CMT, who gave me the opportunity to join his unit.
I would like also to particularly thank my tutor Mr Thomas Perrier, research engineer in the team, who directed my work and knew to dedicate some of his time to help me all along my internship.
I am grateful to Mrs Amandine Andrieux , Mrs Claude Chartier and Mr Pierre Lavenus who initiate me into clean room works, training me on the different equipment in the clean room and who never hesitate to dispense their precious advice in case of issues or doubts.
Finally, I would like to express my gratitude to all the PhD students, apprentice and trainees that contributed a lot to the great atmosphere during the internship: Lucas Bonnin, Paul Chapellier, Léopold Delahaye, Hugo Fafin, Vincent Malesys, Margot Morlans, and Andrea Theault.

Table of contents

Glossary

ANR:	Agence Nationale de la Recherche
AFM:	Antiferromagnet
EDS:	Energy Dispersive Spectroscopy
FM:	Ferromagnet
GNSS:	Global Navigation Satellite System
GPS:	Global Positioning System
Hc	Coercive field
MEMS:	MicroEletroMechanical System
Mr:	Remanent magnetization
Ms:	Magnetisation at saturation
ONERA:	Office National d'Etude et de Recherche Aérospatial
SEM:	Scanning Electron Microscopy
TED:	ThermoElastic Damping

List of figures

Introduction

My master thesis project took place within the ONERA in Châtillon. During these twenty two weeks, I joined the CMT (Capteurs et Micro Technologies) team belonging to the Physic Department of the ONERA. My team is specialized in the development of MEMS (MicroElectroMechanical System) inertial sensors from the theoretical concept and simulations to the implementation with electronics including the realization of the process in clean room. The team is directed by Raphael Levy a doctor engineer and counts sixteen people: 6 PhD students, 7 engineers and 3 lab technicians.

In the beginning most of the projects of the team were based on quartz resonating sensors used as gyrometers and accelerometers. Today the research field of CMT is broadening, in particular with the development of time reference resonators, magnetometers and more recently the study of promising materials such as GaAs for a 3 axis gyrometers or 2D structure such as the graphene to develop gas sensors.

My work was based on the development of a magnetometer in keeping with the PhD of my supervisor Thomas Perrier. One the one hand, I have been involved in the characterization of the resonators designed by the team but also resonators used as differential accelerometers. All those oscillators are complex suspended structures fabricated from quartz wafer. Those characterizations include electrical tests, mechanical stimulations and material structure analysis. On the other hand my work consisted also in improving a new clean room process dedicated to study the magnetic properties of stacks of magnetic materials deposited in stripe shapes. The objective was to identify an optimized geometry that would be particularly adapted for magnetic field detection. Finally this process would complete the fabrication of magnetometers.

Magnetic sensors occupy a significant part of the sensors produced and used worldwide. These sensors are found in many different fields such as automotive, daily life electronic devices, healthcare and of course in the aerospace field where the ONERA carries its research [1]. In a first section, I will introduce the concept of magnetometers, presenting the state of the art, the working principle and the device developed at the ONERA. In a second part, the different studies carried to improve the performance of the sensor will be described. Finally, I will emphasize the clean room process I studied and improved during my internship.

Short presentation of the ONERA

The ONERA (Office National d'Etudes et de Recherches Aérospatiales) is a French aerospace research center that have a public status but also a commercial and industrial aspect (EPIC). It counts several facilities in France and employing around 2000 engineers, researchers and technicians [2]. Its objective is to develop research in the aerospace field according to the need of the industry. It includes the first work of research until the transfer of a device or technic to mass production with national or international partners.
The ONERA is divided in seven scientific departments and my team is part of the DPHY (Département Physique Instrumentation, Environement, Espace). This department focuses on technology including microtechnologies to develop devices dedicated to the aerospace field; for instance, monitoring earth related phenomena or merely for guidance and positioning.[3]

I- Magnetometer

1. State of the Art of Magnetic Sensors

A magnetometer is a magnetic sensor involved in the characterization of a magnetic field. They are divided in two types: scalar (or total field) magnetometers that measure the magnitude of the fields and vector magnetometers measuring one or several vector components of a magnetic field [1].
A large part of vector magnetometers exploits well known macroscopic physical effects. For example, the Search-Coil magnetometers used in harsh environment in the aerospace field, the Fluxgates magnetometers [4] present in aircraft compass systems: both of them rely on the Faraday's law of induction. In the same vein, one can mention the Hall Effect sensors exploiting this effect in semiconductors to detect magnetic field [5]. Despite the poor precision of these devices, those latter have the advantage of being light, quite cheap and can operate within a wide range of temperature. This explains why those sensors are widely used nowadays. Another type of magnetometers relies on magnetic materials. For example, SQUID (Supaconducting Quantum Interference Device) sensors rely on super conductive magnets and is the most sensitive magnetometers for measuring low frequency magnetic fields (<1Hz)[1]. The counter part of this huge accuracy is that the device requires cryogenic refrigeration which leads to high power consumption and a heavy equipment. On the other hand, magnetoresistive magnetometers are much more simple devices, the external field being measured through a change in resistance of the material. This simplicity has a direct impact on the price of the devices which is quite low. These devices exist under several variations that will not be presented in detail here: Anisotropic Magnetoresistance (AMR) sensors, Giant Magnetoresistance (GRM) sensors [6], Magnetic Tunnel Junction (MJT) sensors, Extraordinary Magnetoresistance (EMR) sensors. Giant Magnetoimpedance sensor (GMI) is composed of a wire whom impedance highly depends on the frequency of the current passing through it and on the external magnetic field [7].
The current trend tends to miniaturized all existing system as it can be seen in [8] and [9] with the Hall Effect sensor, where materials with promising properties are studied to design a miniaturized device. The elaboration of MEMS magnetometers follows the same trend, with the objective to produce a large amount of low cost sensors with a high sensitivity, high reliability and low power consumption. MEMS magnetometers are also vector magnetic sensors, measuring the intensity of magnetic fields. However, the main drawback of those sensors is their high sensitivity to rotation speed and vibrations.
Finally, concerning the total field magnetometer, it exists only a few technics that allows to determine precisely both direction and magnitude of the magnetic field. Those methods exploits cold atoms properties and requires huge facilities[10].

This internship is the continuation of an ANR research project on the magnetometer called MAGRIT, which was a partnership between the ONERA, the "Centre de Nanosciences et de Nanotechnologies de l'Université Paris Saclay" and a SME company: Sysnav. The main objective of this project was to design a vibrating magnetometer for indoor positioning purposes. Nowadays, most of our positioning systems rely on GNSS (Global Navigation Satellite System) such as the GPS. However, the GNSS coverage is not effective or not possible in some areas such as building or tunnels. This is where inertial positioning takes over and is able to give an accurate position knowing the starting point. The company Sysnav is able to exploit magnetometers to calculate a 3D speed and compensate the inner long time

drift of accelerometers and gyrometers. Other applications are possible involving magnetometers network for area surveillance.

After this short presentation of the state of the art of the magnetometer and the application targeted by the MAGRIT project, the working principle of the magnetometer as a resonator will be described.

2. Theoretical model of a quartz resonator

Since magnetometers developed at the ONERA are resonators it is important to describe first the model of a quartz resonator and its working principle. A quartz resonator can be described with lumped elements: a mass M attached to a spring in parallel with a damping element. However, it is also interesting to draw an analogy with the electrical domain and consider the equivalent electrical circuit. Piezoelectric resonators like the one I characterized can be represented by the following model: a resistor Rm, a capacitor Cm and an inductor Lm in series shunted by a second capacitor C_0 (see Figure 1).

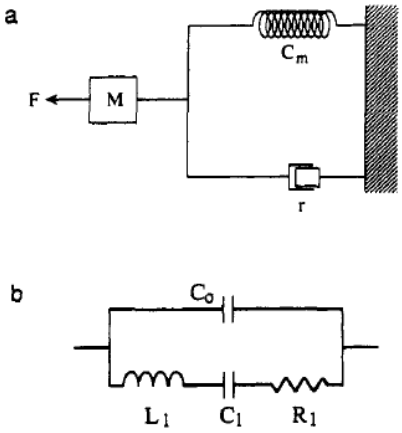

Figure 1: Equivalent mechanical (a) and electrical model (b) of a quartz resonator (extracted from [11]**)**

The three elements in series represent the motional part of the resonator and a parallel can be established between the two models. L1 is the inertial elements corresponding to the mass M of the mechanical system. As the spring, the capacitor C1 stores energy during the oscillations and the value of the capacitance can be associated to the compliance of the quartz Cm, Cm being the inverse of the stiffness of the spring. Finally R1 represents the dissipation of the energy during the oscillation exactly as the damping element r. This equivalence between the different parameters can also be emphasized establishing the equation of the motion of the mass M and the equation of the electrical circuit.

Mechanical domain equation:

$$M\ddot{x} + r\dot{x} + \left(\frac{1}{Cm}\right)x = F \tag{1}$$

x is the displacement of the mass and F the excitation force

Electrical domain equation:

$$L_1\ddot{q} + R_1\dot{q} + \left(\frac{1}{C_1}\right)q = V \tag{2}$$

q is the electric charge and V the excitation potential

The capacitor C_0 has been added to the electrical model to take into account the static capacitance due to the presence of the electrodes that actuate the resonator.[11] The equation (1) can be rewritten using the basic form of the equation of an oscillator with Q the quality factor and ω_0 the eigenfrequency of the resonator:

$$\ddot{x} + \frac{\omega_0}{Q}\dot{x} + \omega_0^2 x = F/M \tag{3}$$

Exploiting the analogy with the electric circuit, it is possible to deduce the expression of Q and ω_0 comparing the equations (2) and (3). It gives:

$$\omega_0 = \sqrt{\frac{1}{L_1 C_1}} \tag{4}$$

$$\mathrm{Q} = \frac{1}{R_1}\sqrt{\frac{L_1}{C_1}} \tag{5}$$

Q represents the ratio between the energy stored in the system and the energy lost. It includes five main different mechanisms:

$$\frac{1}{\mathrm{Q}} = \frac{1}{Q_{defects}} + \frac{1}{Q_{TED}} + \frac{1}{Q_{viscous}} + \frac{1}{Q_{anchor}} + \frac{1}{Q_{viscoelastic}} \tag{6}$$

where:

- $1/Q_{defects}$ includes all losses concerning the material defects, for example irregularities in the crystal lattice.
- $1/Q_{TED}$ refers to the thermoelastic damping (TED). This phenomenon consists in the apparition of a temperature gradient due to the dissipation of heat created by the vibrating parts of the system. [12][13]
- $1/Q_{viscous}$ corresponds to the dissipation of energy related to the environments of the resonator. This term is null when working in high vacuum.
- $1/Q_{viscoelastic}$: takes into account the dissipation due to strain variations in non-crystalline gold electrodes.
- $1/Q_{anchor}$ concerns the design of the resonator itself, in particular losses of energy at the anchors.

The expression (6) emphasizes the different contributions to the energy losses in the resonator. The work carried out during the internship focuses on TED and viscoelastic losses. Now that the basis of the theory of the resonator is set, it is possible to present the magnetometer designed by the CMT team.

3. Magnetometer developed at the ONERA

a) General presentation of the device

The magnetometer is a quartz resonator on which magnetic materials has been sputtered. The working principle is illustrated in Figure 2 and consists in a constant excitation

of the device at its resonance frequency. In presence of an external magnetic field the stiffness of the vibrating parts is modified due to the magnetostatic torque and a shift in the resonance frequency is observed.

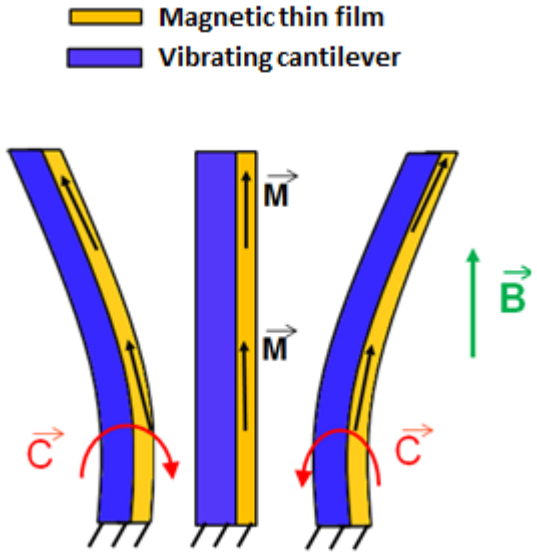

Figure 2: Vibrating cantilever magnetometer in flexion (taken from [14]**)**

Since the shift Δf is proportional with respect to the applied magnetic field B it is possible to deduce the value of this latter from the measurement of the shift in frequency: Δf = K*B. K is the scale factor or sensitivity of the sensor and depends on the vibrational mode of the resonator and of the position and remanent magnetization of the magnetic thin film on it [15]. The MEMS developed by the CMT unit presented in the Figure 3 is a quartz resonator exploiting the torsional mode of vibration. It is constituted of a transversal suspended beam that maintains in the middle two perpendicular arms terminated by a paddle. Hard magnetic material is sputtered on the two paddles and allows the detection of magnetic field. The whole structure is very fragile and must be handled with care. On a 3x3cm^2 quartz wafer, 20 cells are fabricated.

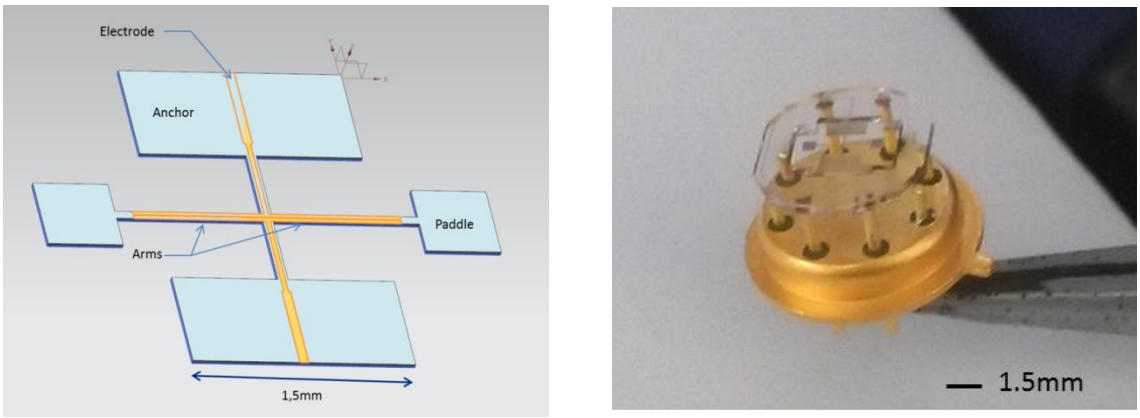

Figure 3: On the left model of the torsional resonator designed on SimCenter. The resonator is held at the end of the anchor rectangles. On the right is a picture of a magnetometer cell mounted on a supporting base.

Most of the time, the cells are directly tested on the wafer to make the manipulation easier. Indeed, gold electrodes are designed along the arms up to a side of the wafer. This allows to interact easily which each cells, in particular the one situated in the middle of the wafer. The particularity of this resonator is that the studied vibrational mode of the arms is the torsional

one. Each paddle is rotating around the axis formed by the arms; the paddles experience an anti-phase vibration.
At this state of the development, the objective is to study the device as a simple resonator and to identify the most efficient geometry. That is why on the wafers produced at this time, there are eight different versions of the resonators with different sizing for the lateral arms and paddles.
The next section presents the figures of merit of the resonator.

b) Figures of merit

A paper published by the unit [16] illustrates the performances and limits of a sensor with a frequency output, exploiting its Allan variance. This variable is used to evaluate the noise behavior according to the observation time of a resonator and is presented in Figure 4.

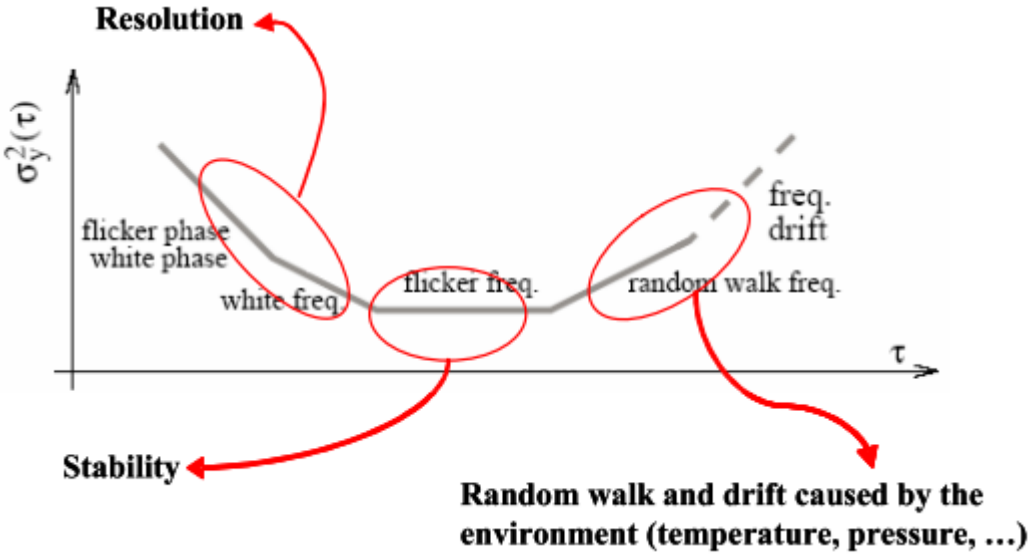

Figure 4: Allan variance $\sigma^2(\tau)$ from [16]

The phase noise described by the Allan variance allows different kind of noises to be identified. The white phase noise corresponds to the background noise and reducing it enhances the resolution of the sensor. Then, the Flicker noise is mainly due to the reading electronic of the device and influences the stability of the measures. The third kind of noise corresponds to environmental variation on the long term involving common mode effects such as temperature or pressure. Since this noise can be suppressed using a reference or a differential measurement, two sources of noises remains. The Allan deviation is the square root of the variance and can be expressed for the different regions:

Resolution:

$$\sigma(\tau) = \frac{\sqrt{3FkTf_H}}{\sqrt{P_0}2\pi.K}\frac{1}{\tau} \tag{7}$$

Stability:

$$\sigma(\tau) = \sqrt{\frac{\ln(2)b_{-1}}{2}}\frac{f_0}{Q.K} \tag{8}$$

Where T is the temperature, f_H is a cutoff frequency, F is the amplifier noise figure, b_{-1} is the amplifier Flicker phase noise, P_0 the carried power, f_0 the resonance frequency of the oscillator, Q the quality factor and K the scale factor expressed in $Hz.T^{-1}$.

According to the expression (7), if one wants to mitigate the white noise and improve the resolution, the scale factor must be improved. The same concerning the stability expressed in (8), minimizing the Flicker noise is equivalent to increase both the quality factor and the scale factor.
The quality factor is the first parameter to be maximized. This is done through the design and the elaboration of the geometry of the device. Then the scale factor must be optimized improving both sensitivity and stability. Since we are dealing with a magnetometer, K is proportional to the remanent magnetization M_r of the magnetic material and V_{mag} is the total volume of deposited materials:

$$K \propto K_{geo} M_r V_{mag} \quad (9)$$

with K_{geo} a geometrical parameter, deduced by finite element analysis.
The relation (9) explains the choice of the magnetic materials has a direct impact on the performances of the magnetometer. To improve both stability and resolution, the two parameters to maximize are the quantity of deposited metals and the value of the remanent magnetization. Moreover, the scale factor must remain stable. Its stability depends on the stability of the remanent magnetization Mr as regards magnetic field fluctuations, which improved when the coercive field is strong. Thus, maximizing Hc stabilizes K.
This section emphasized the key parameters of the magnetometer. Its performances can be enhanced by maximizing the quality factor -playing on the geometry of the design- but also the scale factor which value and stability depends on the quantity and magnetic properties of the materials involved. The choice of the magnetic material is justified in section III-1). In the next section are presented simulations that allow to obtain the different key parameters for a given device.

c) Simulation

As explained previously, the magnetometer is a based on a resonator. At certain precise frequencies, the MEMS may experience a resonance phenomenon involving different types of motion according to the resonance frequency. These are called eigen modes. Concerning the magnetometer designed by the unit, the interesting mode is the torsional mode. Thanks to a DAO software (Simcenter GUI coupled to the OOFELIE::Multiphysics Solver) it is possible to identify at which frequency the torsional mode is experienced by the device. In order to study the magnetometer, I designed one of the existing resonators. My objective was to retrieve the theoretical values of the resonance frequency and then the quality factor that were provided to me. The first simulation is a modal analysis. The Figure 5 presents the sixth mode of resonance around 25kHz.

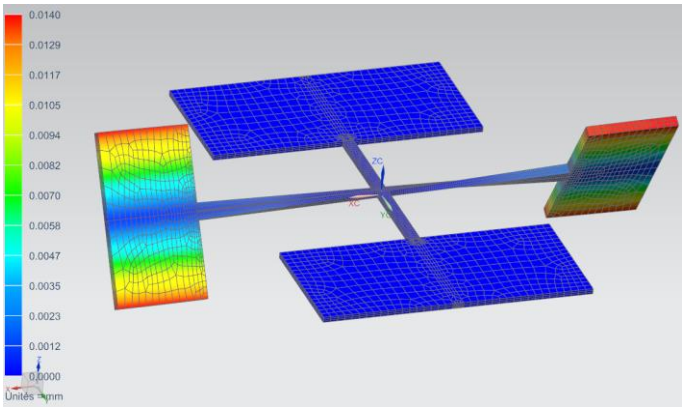

Figure 5: Torsional mode of the resonator (magnified view taken from Simcenter software)

The second step is to realize a harmonic analysis that allows the theoretical value of quality factor of the resonator to be obtained. Realizing a sweep in frequency around the resonance frequency it is possible to trace the displacement of one paddle according to the frequency applied on electrodes. In this case, I only consider the thermoelastic damping neglecting all the other losses of energy: at the anchor, due the electrodes, the presence of defects or viscous damping related to the environment.

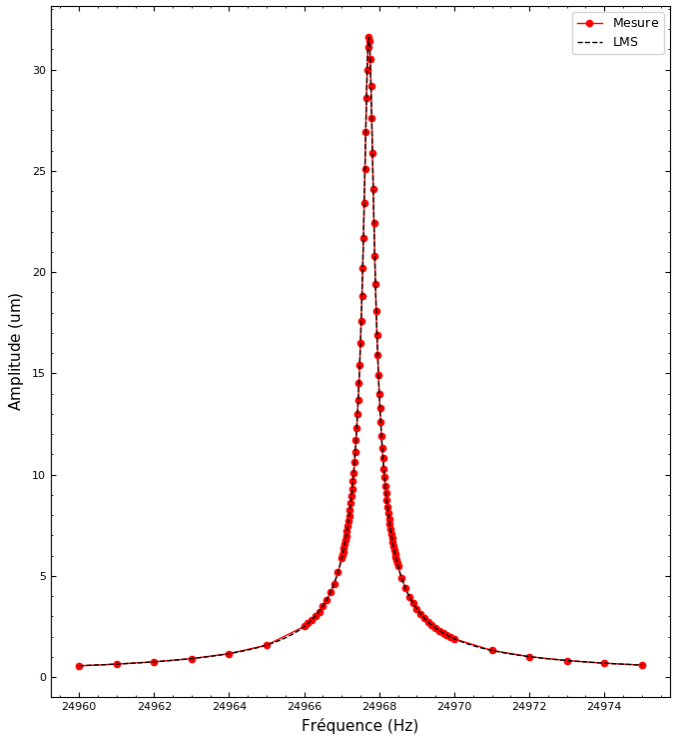

Figure 6: Displacement of the paddle according to the frequency. The LMS dashed line is a fit using a least mean square algorithm of a lorentzian

The plot of the Figure 6 is obtained by following the position of one point situated at the end of one of the paddle. Near the resonance frequency and for high quality factor this resonance behavior can be described by a Lorentzian model (see Appendices for detailed explanations). Using the equation (10), a fitting curve can be established.

$$X^2(\omega) = \frac{X_{max}^2 \left(\frac{\omega_0}{2Q}\right)^2}{(\omega - \omega_0)^2 + \left(\frac{\omega_0}{2Q}\right)^2} \quad (10)$$

The simulation corresponds perfectly with the fit and allows the quality factor of the resonator -around 81000 in this case- and the exact resonance frequency: 24967.72Hz to be determined

In addition to the resonance frequency and the quality factor, the scale factor can also be obtained through simulations. As it has been discussed in the previous section, the scale factor is a critical parameter of the magnetometer and must be optimized to enhance the performances of the device. The operation would consist in a first modal simulation to identify the resonance frequency. Then, the same simulation is performed but this time adding a perturbation in the vibrational motion taking into account the presence of an external magnetic field B. This allows to identify a shift of the resonance frequency Δf. Since Δf is linked to the scale factor by the relation $\Delta f = K.B$, it is possible to evaluate the scale factor K. Moreover, it has been said that scale factor K is also proportional to the remanent magnetization M_r of the material present on the device, the volume of deposited metal V_{mag} and a coefficient $K_{géo}$ depending on the geometry of the resonator. Knowing the first two parameters, it is possible to evaluate K_{geo}.

This part presented design of the resonator dedicated to the elaboration of a magnetometer. It also described the simulations to perform to evaluate the figures of merit of the magnetometer. The next section explains the work realized to improve the quality factor of tested resonators.

II- Improving the quality factor

1. Influence of a thermal treatment on the quality factor

In order to test some magnetometers, I have been trained by my tutor on different experimental set up. First, the objective is to determine the resonance frequency of torsional magnetometers at atmospheric pressure. The experimental set up consists in a two-probe measurement to record electrical impedance of each mechanical resonator. When tested, the resonators are still attached to the wafer to simplify the manipulation.

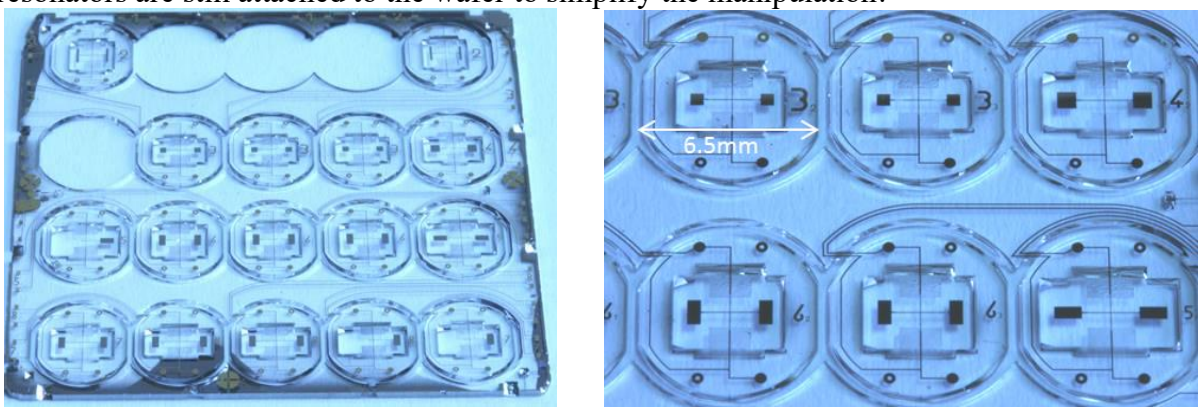

(a) (b)

Figure 7: (a) 3x3cm wafer of resonators and (b) a zoom on six resonator cells

The Figure 7 (a) presents the kind of wafer I manipulated. In Figure 7 (b) it is possible to see that the dimension of the paddle varies from a cell to another. Concerning the measurements, two tips are placed on the electrodes and the impedance analyzer displays the modulus and the phase of the transfer function of the resonator. Knowing the theoretical resonance frequency, a scan is realized in a range of several kHz around this value. When the resonance is localized it is possible to perform a least mean square fit with the instruments using the equivalent electrical model of a mechanical resonator that was described in the previous section: a RLC circuit in parallel with a capacitor C0. The apparatus gives directly the value of the different elements and thus allows determining the resonance frequency and the quality factor of the structure. In practice, the resonance frequency is always found to be superior to the theoretical one of several kHz, due to a thickness which is greater than the one used during simulations. Nevertheless, the obtained Q factors are very low because we are operating at atmospheric pressure. This experiment stays relevant since it allows roughly determining the resonance frequency of each device and identifying the functional cells.

The next step consists in performing the same measurement but this time under vacuum. The electrodes of each devices of the wafer are connected to a PCB support composed of several ports (see Figure 8).

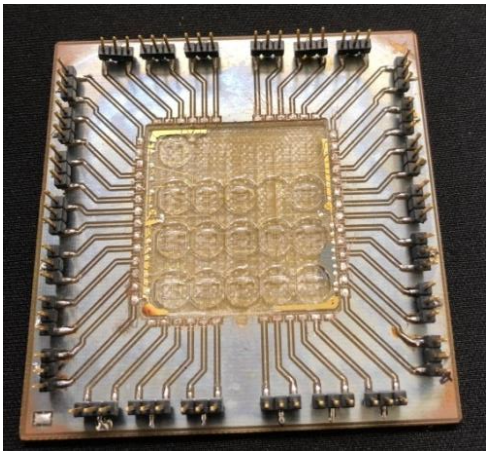

Figure 8: Wafer of resonators set on a PCB. Gold wires are used to connect each device

The wiring is done by means of thin gold wires and conductive silver glue. This allows monitoring each resonator easily using directly the ports of the PCB to interact with the devices and in particular to perform measurement under moderate vacuum (10^{-5} mbar). The equipment used is presented in Figure 9.

Figure 9: Resonance measurement under vacuum: a dry pumps and a molecular pump are used

Those measurements are carried with an impedance analyzer (see Figure 10) exactly as previously but this time the objective is to eliminate the viscous damping due to air in order to get closer to the theoretical value of the quality factor. As in the first measurements, the apparatus is able to realize a fit of the collected data with a given model.

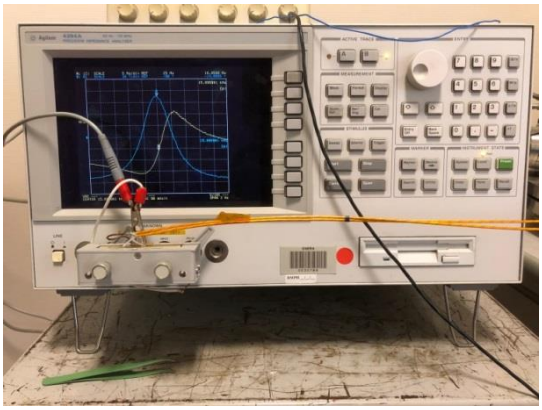

Figure 10: Impedance meter displaying typical signals at resonance, the blue signal corresponds to the phase and the yellow to the modulus of the transfer function

However the fitting model proposed by the instruments is not very efficient for high quality factor. All the data are analyzed in a second time thanks to a least mean square fit, implemented in the Python language by the team. On the Figure 11 one can observe a typical curve obtained for a resonator after fitting:

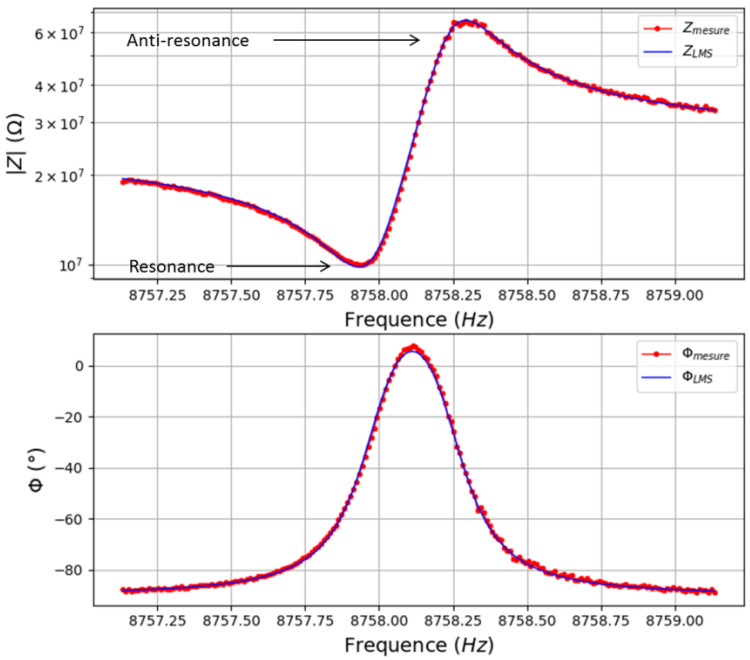

Figure 11: Impedance and phase measurement of the torsional resonator 8_3 under vacuum, fitted with the least mean square method (LMS)

Even if it is possible to observe an improvement of the quality factor by operating the device under vacuum, the Q is still less than half of the theoretical value. For instance, with the resonator of the Figure 11, there is a mismatch of 75% with the theoretical value that reaches 91000. A large part of the work I carried out during my internship was to figure out why there were such differences between theory and reality and how to improve the quality factor of the device.

First, it has been found that realizing a thermal treatment on the wafer on a hot plate, around 230°C for 15 min, increases significantly the quality factor of the resonators (several thousand units). The setup elaborated for the annealing step is illustrated in Figure 12.

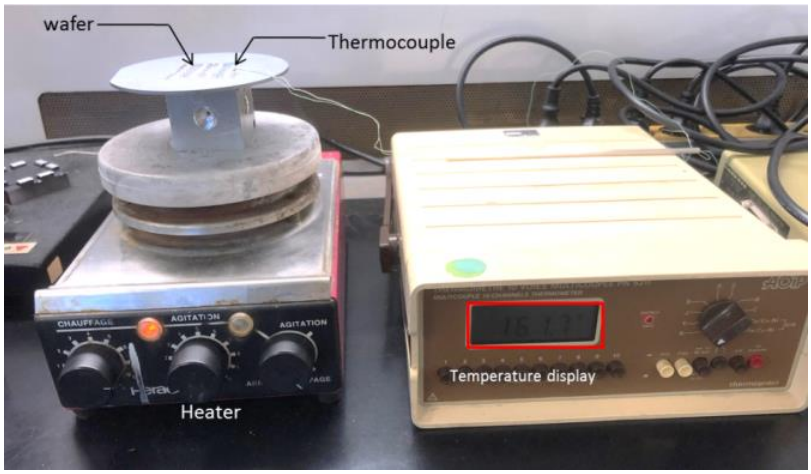

Figure 12: The wafer is annealed in order to improve the quality factor of the resonators and the temperature is controlled with a thermocouple

The wafer is wired a second time to the PCB and measures are performed inside the vacuum chamber. An increase of the quality factor is noticed, the values are multiplied by a factor between 1.2 up to 4 after the thermal annealing. (see Figure 13)

reference	Q theorique	Q	Q	Q after thermal annealing	Improvement due to the bake	Mismatch to the theoretical value
		atm	vacuum	vacuum		
11	63617					
12	63617					
13	63617					
21	35692	40	19161	25399	33%	29%
22	35692					
31	81347	1113	21629	41270	91%	49%
32	81347	671	33502	50815	52%	38%
33	81347					
41	60233	775	27274	40783	50%	32%
42	60233	216	25463	41918	65%	30%
51	67524					
52	67524	365	28366	46746	65%	31%
61	61027	63	27617	43798	59%	28%
62	61027	174	27286	40245	47%	34%
63	61027	239	24581	37135	51%	39%
81	89504	788	11533	52723	357%	41%
82	89504	616	17838	34127	91%	62%
83	89504	272	22184	36103	63%	60%
71	74931	684	25323	37452	48%	50%
72	74931					

Figure 13: Table emphasizing the improvement of the quality factor (the grey cells indicates a non-working cell)

The experiment presented in this part has an important influence on the quality factor of the resonator. The objective of the next section is to explain this behavior.

2. Identification of the damping sources compensated by the bake

Different hypothesis have been considered by the team to explain this tremendous improvement. Three causes have been studied during the internship and are discussed in the three next parts.

a) Adsorption of gas

First of all, it has been proposed that baking the resonator would induce a desorption of molecules by the quartz surface. Indeed, it would be possible that, with time, the quartz surface adsorbs gas molecules present in the atmosphere [17][18]. However, several tests have been realized over the time: when tested a few months after, the quality factor did not change and the hypothesis of the absorption was rejected. In the Figure 14, it can be seen that quality factor is constant over time for three different cells.

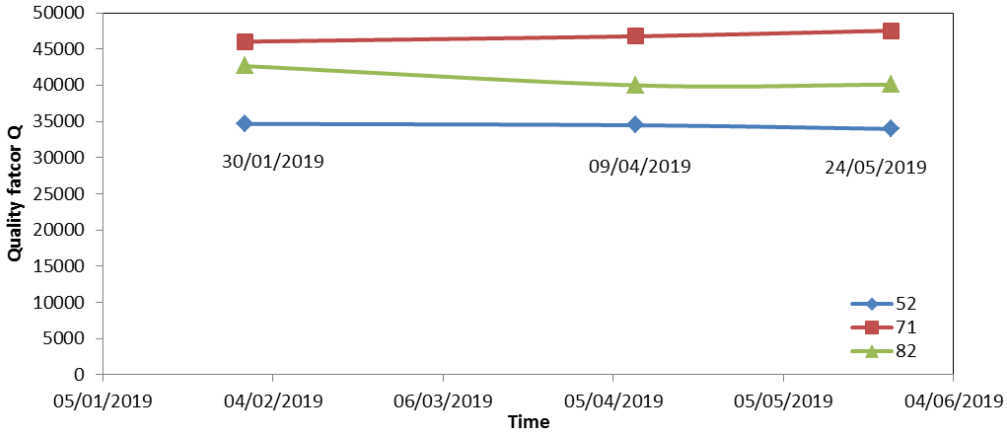

Figure 14: Evolution of the quality factor over four months of three resonators

Since the quality factor remains constant over several months, the hypothesis of gas absorption by the quartz substrate has been dropped.

b) Impurities on the surface

Then, it has been thought that organics impurities such as traces or thin films of resist could be still present on the surface of the resonator at the end of the process. These impurities would cause viscoelastic losses and thus lower the quality factor of the resonator. A thermal treatment could clean the surface and improve the performances of the device. Nevertheless, observing the different resonators with the optical microscope did not allow finding any traces on the surfaces. That is why Raman spectroscopy has been used. This apparatus can provide a precise analysis identifying chemical bounds present on a surface. Performed on a resonator before and after the bake, the analysis is presented in the Figure 15: Both the obtained spectra are identical and typical of the one of the quartz found in the literature [19].

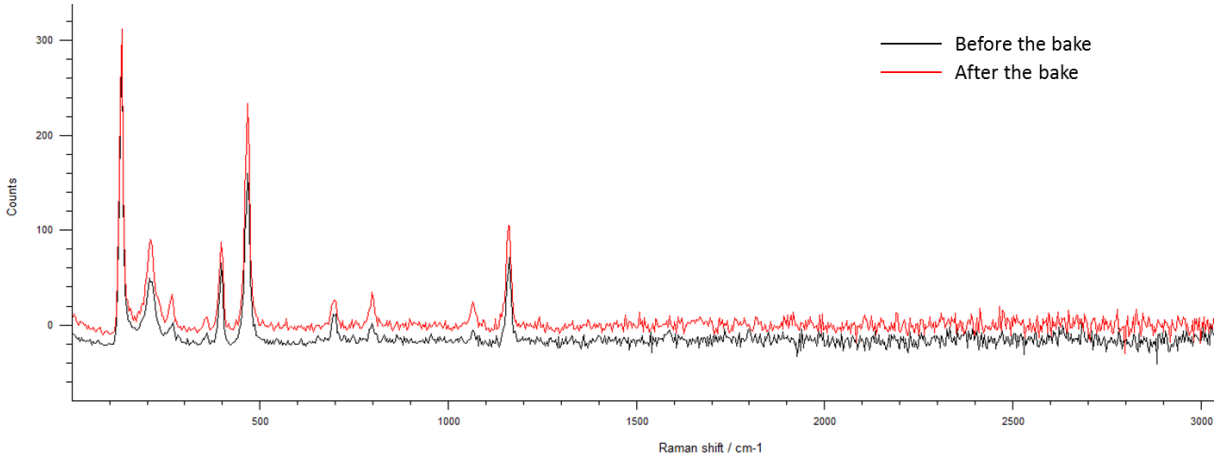

Figure 15: Raman spectra before and after a thermal annealing of the resonator

Again, the possibility of the presence traces of resist or other contamination has been dismissed.

c) Modification of the electrode lattice structure

The resonators are fabricated starting from a quartz wafer coated on both side by gold and chromium. These layers are etched during the process to form the electrodes of the device. The last option would be a rearrangement of the crystalline microstructure of the gold electrodes during the bake. This hypothesis is maintained by an intern research carried by the unit on the chromium (15nm)/gold(200nm) layer deposited on a quartz substrate by e-beam evaporation. In this report, the influence of a thermal annealing is studied. The gold layer presents a micro granular surface after evaporation. The experience consists in baking the substrate at different temperatures: 100°C, 200°C and 400°C during 4 hours. The interesting results are obtained at 200°C, the size of the grains tends to increase significantly comparing with the image of the witness. This can be seen in Figure 16 with SEM images taken from the report. At 400°C, holes appear in the metallization during the first hour.

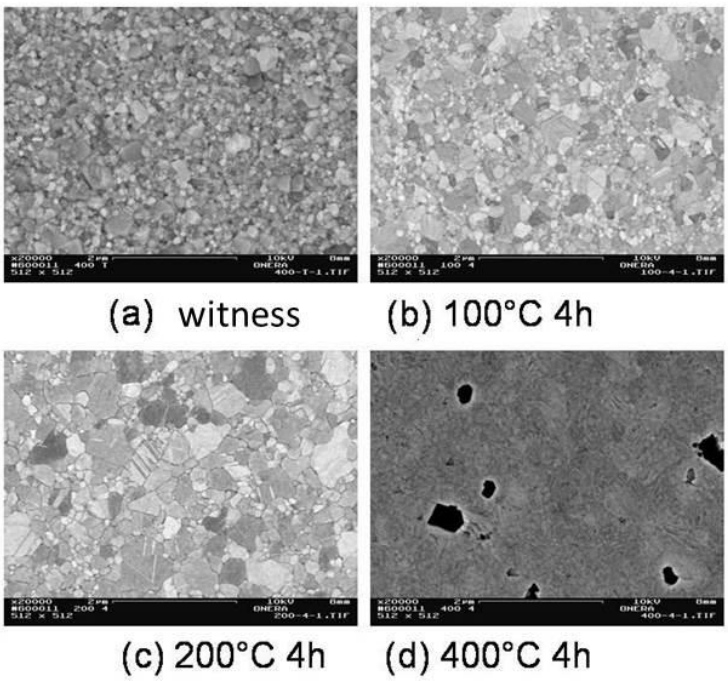

Figure 16: SEM images of the gold layer after four hours of bake at 100°C, 200°C and 400°C

Considering the evolution of the structure of the gold electrodes, large grains could induce less friction losses at the interface between gold grains and induce an increase of the quality factor of the device. Despite this improvement of the quality factor, this later remains far from its theoretical value, so all losses have not been removed. Moreover, the thermal treatment applied to resonators is last only a few minutes and we cannot affirm that the microstructure is really affected. A SEM analysis must be realized on treated resonators to confirm this hypothesis.
In the next section will be discussed a way to emphasize that electrodes are responsible for the low quality factor of resonators.

3. Impact of the presence of electrodes on the device

In the aim to improve the resonators' efficiency, it has been proposed to study the impact of the presence of gold electrode on the resonator. Indeed, these electrodes could compromise the quality factor of the device by dissipating energy through viscoelastic losses (internal friction of grain boundaries). The idea would be to remove by chemical etching the electrodes of some cells and evaluate their performances comparing to measurements done before etching. This requires an experimental set up able to excite a resonator without electrodes. The clean room of the team is equipped with a Fogale instrument that can mechanically stimulate a resonator with a vibrating piezoelectric support. Thus, it was decided to mount some cells on their base and evaluate their performances. Four cells were prepared to be studied using the optical vibrometer apparatus (Figure 17).

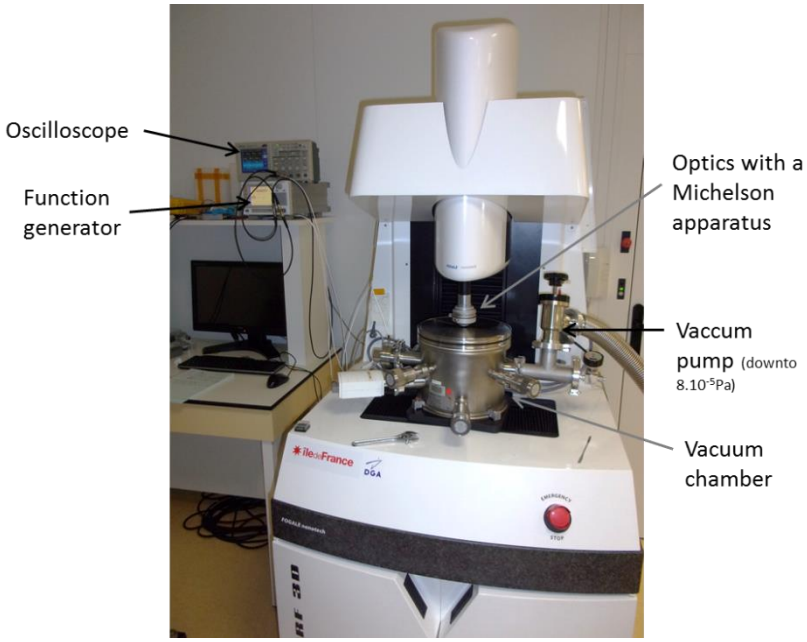

Figure 17: Optical vibrometer apparatus, displacement measurement by optical means

The resonators can be excited mechanically thanks to a piezoelectric base or electrically by wiring the cells. The response is measured by optical means using a Michelson interferometer integrated inside the objective of the optical vibrometer. A camera above the chamber allows setting the apparatus. A red light LED is used to create the interference pattern on one of the paddle. First of all, it has been chosen to excite the resonator using an external electric generator. At this moment of the experiment the electrodes are still present on the resonator. The first objective was to compare the results obtained with the impedance meter and the vibrometer to confirm the relevance of this measure. Then measures would be carried on

resonators whom electrodes have been etched. The Figure 18 presents one of the measures I realized on one of the resonator.

.

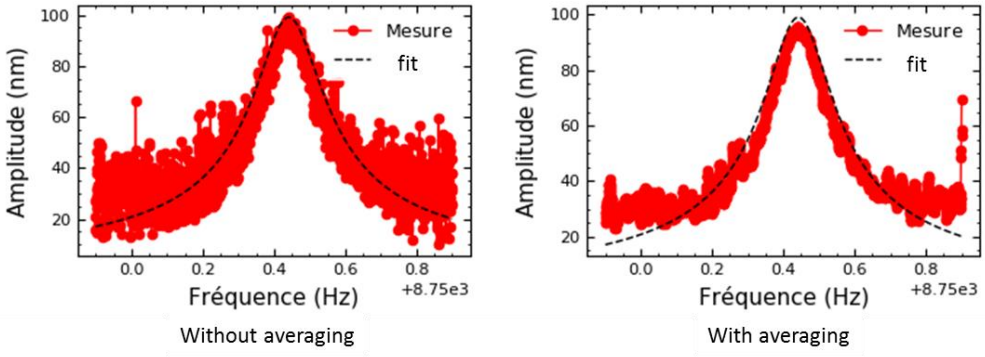

Figure 18: Resonance measured with the Fogale set up on resonator with electrodes. Since the raw data (left) is very noisy, a python script is used to smoothen the curve and obtain the one on the right.

Extracting the data and using a script in Python allows to create a fit of the curve and determine the different figures of merits of the resonator in particular its quality factor. As is may be noticed, the background is very noisy representing almost one third of the signal on the left trace. Indeed, the measurement is very sensitive: this is due to the fact that the Fogale apparatus uses a LED to create the interference patterns on the motion part of the resonator. An image processing on the contrast between the different fringes allows obtaining the displacement of the paddle. This explains the heavy noise during the recording: the least motion or shock near the machine can modify the interference pattern contrast. Despite all the time dedicated to these measurements it was not possible to obtain reproducible results, the measurement conditions need to be improved by lowering the noise level around the apparatus. Moreover the machine broke down during the test phase and I was not able to begin the second part of the experiment: the study of the resonators without electrodes.

Later, an external company came at the ONERA to propose an optical measurement through laser vibrometry means similar to the one of the Fogale machine. I had the opportunity to attend a demonstration on the resonators previously studied with the optical vibrometer. On the contrary to this later, the new method relies on a red laser using Doppler Effect to measure the mechanical displacement of the paddle and is not sensitive to vibration. Despite the noisy environment of the clean room and the poor experimental conditions, the results were much better than the one obtained by the optical vibrometer. Since the resonators were still in the vacuum chamber of the Fogale apparatus, a mirror was used deviate the laser into the chamber. The Figure 19 emphasizes the result obtained by piezoelectric stimulation of the resonator.

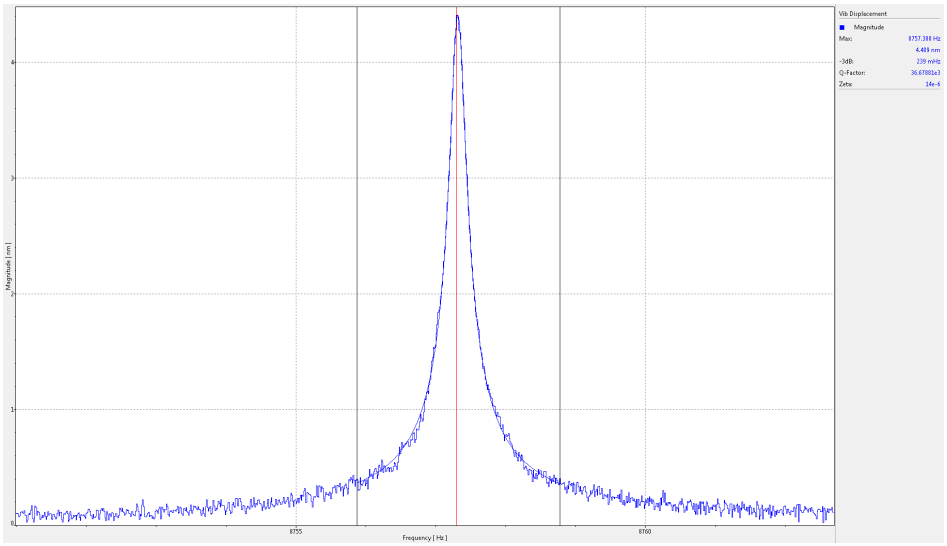

Figure 19: Resonance peak on a torsion magnetometer detected by laser vibrometry (x_axis: frequency in Hz/y_axis: displacement in nm)

The curve has a lorentzian-like behavior that I was not able to observe easily with the Fogale optical vibrometer. In addition the signal to noise ratio is really good compare to the one of the Fogale. The same profile has been observed several times using the same acquisition parameters assuring the reproducibility o the measurement. Moreover, the quality factor measured matches with the results I obtained with the impedance analyzer.

To conclude, these experiments allowed a better understanding of the improvements of the quality factor due to the bake. However, due to unexpected issues it was not possible to explore the impact of the electrodes on the quality factor of the resonator. In the last section will be presented the work carried in clean room.

III- Magnetic Strips Study

This work was the opportunity for me to work in clean room and improve a process. A first part will present how the magnetic materials have been chosen and what justifies the elaboration of a clean room process. This latter involves different technics specific to the clean room that will be presented in a second part. From these explanations it will be possible to detail the steps of the process. In a last part, the evolution of the process will be presented.

1. Magnetic materials

According to the section I-3.-b), the efficiency of this magnetometer relies on the geometry of the resonator but also on the choice of magnetic materials employed for the detection. The sensitivity of the sensor is directly proportional to the remanent magnetization of the magnetic layer. The ideal characteristics for the magnetic material are presented with a hysteresis cycle in Figure 20.

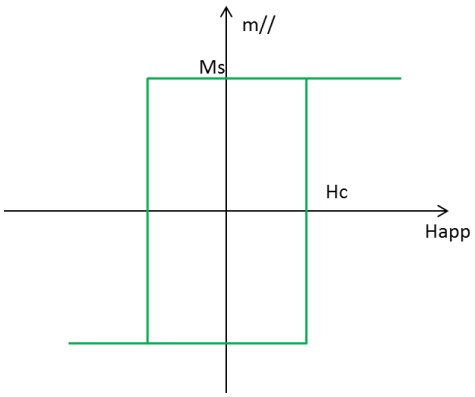

Figure 20: Ideal hysteresis loop for magnetic material in a magnetometer (Ms = magnetization at saturation, Hc Coercive field, Happ = external magnetic field, m// = magnetization along the easy axis)

It presents a high remanent magnetization to maximize the resolution of the device and an important coercive field as well to ensure a good stability and avoid the reversal of the magnetization. As it can be seen in [20] and [21], rare earth elements such as NdFeB or SmCo would perfectly fit the role of magnetic material in a magnetometer. However, it appears rapidly that these elements are not suited at all for this application. Indeed, there high internal tensile strain prevents the deposition on quartz substrate. In addition, rare earth elements present a low Curie temperature and low resistance to oxidation which make them impossible to use in harsh environments.
Finally, it was decided to focus on stacks of thin layers of ferromagnetic (FM) and antiferromagnetic (AFM) materials involving exchange bias at the interface between each layer. This allows to use more common magnetic materials:

- Iron-Cobalt alloy has been chosen for its ferromagnetic properties presenting a strong magnetization at saturation as well as a high stability of its remanent magnetization with respect to external magnetic field (Mr/Ms close to 1).
- Nickel-Manganese (NiMn) has been adopted for its antiferromagnetic characteristics and in particular for its resistance to oxidation and its high exchange energy J_{Ex} ($J.cm^{-2}$) which is quite stable with respect to the temperature [22].

Exchange bias interactions in a magnetic stack have the particularity to shift the hysteresis cycle when a magnetic field is applied along the easy axis. This particularly is appreciated since we need a constant and maximum magnetization for small external magnetic field. In

this case, the coercive field does not need to be important anymore. On the contrary, Hc must be minimized so that the magnetization would remain stable on a larger range. The hysteresis cycle would approach the one of the Figure 21.

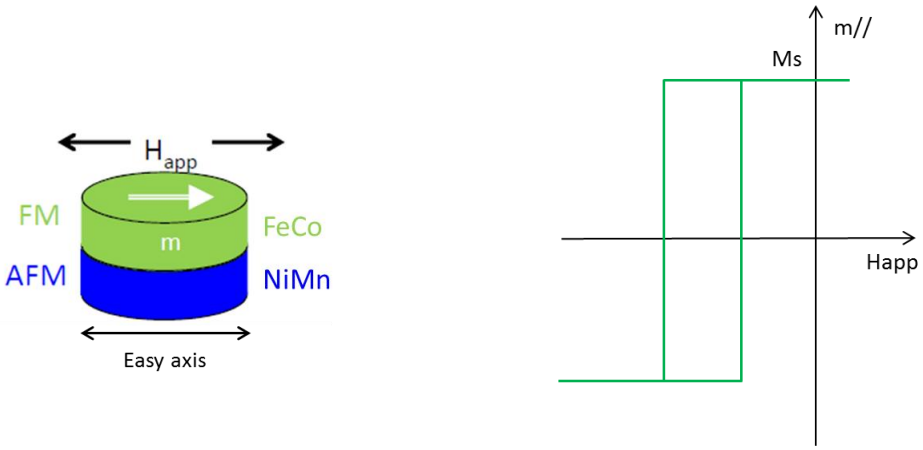

Figure 21: One the left is illustrates the interface between AFM and FM (adapted from Spintronics course). On the right is the ideal hysteresis cycle corresponding to the stack. The exchange interaction at the interface shifts the cycle towards the left.

The magnetic interaction between the two materials can be described by the Stoner Wohlfarth model [21]expressing the total energy of the system as:

$$E_{tot} = E_{Zeeman} + E_{MCA} + E_{dem} + E_{Ex} \quad (11)$$

In the equation (11), the Zeeman energy, E_{Zeeman}, represents the interaction between the ferromagnetic layer and the external magnetic field H. The term E_{MCA} takes into account the magnetocristalline anisotropy of the structure. E_{Ex} characterize the exchange bias at the interface between the two materials. Finally, E_{dem} illustrates the demagnetization field. The last term is supposed negligible with respect to the others since we are dealing with thin layers. According to Meiklejohn [21], in the equation (12) the total energy per unit of area is given by:

$$E_{surf} = -HM_{FM}t_{FM}\cos(\gamma - \beta) + K_{FM}t_{FM}sin^2(\beta) + K_{AFM}t_{AFM}sin^2(\alpha) + J_{Ex}\cos(\beta - \alpha) \quad (12)$$

where M_{FM} is the magnetization at saturation of the ferromagnetic material, H is the applied magnetic field, K represents the crystalline anisotropy energy per unit of volume and J_{EX} is the exchange anisotropy energy per unit of surface. In addition, considering the energy per unit of surface allows the thickness of the antiferromagnetic layer t_{AFM} and the thickness of the ferromagnetic layer t_{FM} to be taken into account.

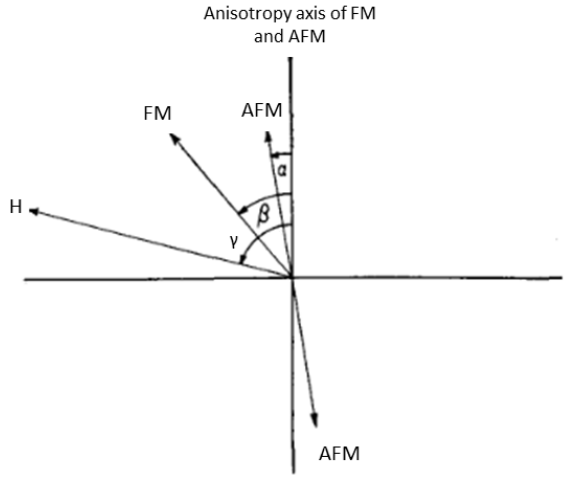

Figure 22: Vector diagram identifying the different angles (adapted from [21]**)**

The angles α, β and γ represented in the Figure 22 correspond respectively to the angle between the magnetization of the FM layer and the anisotropy axis of the FM, the angle between the magnetization of the AFM layer and the anisotropy axis of the AFM, the angle between the applied magnetic field and the anisotropy axis of the FM. It is supposed that the anisotropy axis of the AFM and FM are one unique axis. Moreover Meiklejohn considers that the energy of anisotropy of the ferromagnetic material is negligible. Thus, there are values of α and β in which the system reaches a stable state with a minimum energy. Calculating the partial derivatives of the energy with respect to the angles α and β it gives:

$$\frac{J_{Ex}}{K_{AFM}t_{AFM}} = \frac{\sin 2\alpha}{\sin(\beta - \alpha)} \tag{13}$$

$$\frac{J_{Ex}}{HM_{FM}t_{FM}} = \frac{\sin(\gamma - \beta)}{\sin(\beta - \alpha)} \tag{14}$$

There is a shift of the hysteresis cycle when the magnetocristalline anisotropy is stronger than the exchange energy: $K_{AFM}.t_{AFM} > J_{Ex}$. In the extreme case where $K_{AFM}.t_{AFM} >> J_{Ex}$, it is possible to deduce from equation (13) that α tends towards 0 (for demonstration see Appendices). Finally, considering all the previous assumptions and that H is parallel to the easy axis -meaning γ = 0- the equation (14) can be simplified as follow:

$$\forall\, \beta, \qquad H_{Ex} = \frac{J_{Ex}}{M_{FM}t_{FM}} \tag{15}$$

H_{Ex} is the exchange field expressed in $A.m^{-1}$, it corresponds to the shift of the hysteresis. M_{FM} is the magnetization at saturation of the ferromagnetic material in T and J_{Ex} corresponds to the exchange anisotropy energy per unit of surface. The equation (15) emphasizes that the exchange bias takes place at the interface: when the thickness of the ferromagnetic material increases, the shift of the hysteresis cycle is reduced. This is quite annoying since the sensitivity of the magnetometer is directly proportional to the thickness of ferromagnetic materials. To overcome this issue it was decided in previous works to increase the number of FM/AFM interfaces in the structure by depositing a multilayer stack. The only limit of such a system is the internal stress and the adhesion to the substrate.

However the magnetometer cannot operate directly after the metals have been deposited. Indeed, it appears that when the NiMn is sputtered, the alloy is paramagnetic. To induce a transition toward the antiferromagnetic phase, the stack must be thermally annealed.

In addition, baking the stack under magnetic field allows the spins at the interface FM/AFM and increases the exchange bias to be aligned. The stack is baked at 300°C under a 20 mT magnetic field. Even if this temperature is lower than the Neel temperature of the AFM (T_N = 800°C) and the Curie temperature of the FM (T_C = 920°C), the annealing induces modification of the spin orientation at the interface. During the cooling, the spins of the AFM layer tends to align with the one of the FM at the interface. According to magnetic measurements realized by the team on magnetic stacks composed of several interfaces FM/AFM, the hysteresis cycle obtained are not as sharp as the ideal cases presented previously. The expected behavior of these metals in a magnetometer is a single value of magnetization when the external magnetic is close to zero ensuring magnetic stability. The Figure 23 illustrates well this phenomenon: the cycle is shifted thanks to exchange bias but a null magnetic field corresponds to two different magnetization states circled in black.

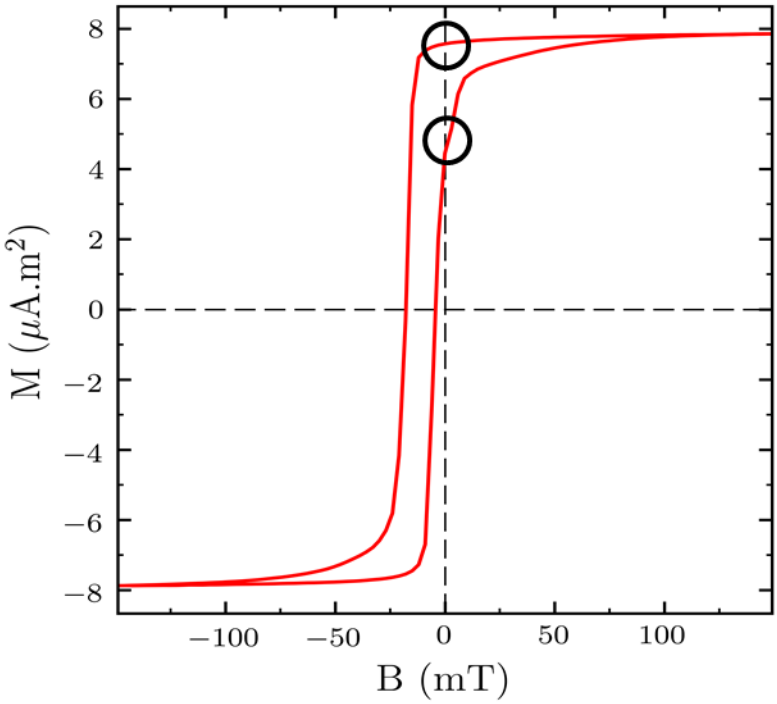

Figure 23: Hysteresis cycle obtain through measurement on magnetic stack

D. Ettelt [23] explains that generating a shape anisotropy makes the cycle more rectangular and improves the stability of the magnetization with respect to magnetic perturbation. This anisotropy can be obtained by playing on the shape of the stack and particular realizing stripes parallel to the magnetization direction. The main objective of the process studied during the internship is to deposit stripes of staked magnetic material of different shape to evaluate the impact of the geometry of the stripes on the hysteresis cycle.

To conclude this section, the chosen materials have complementary properties: the NiMn is stainless and protect the FeCo from oxidation, FeCo presents a strong magnetization at saturation and a multilayer stack allows increasing the exchange bias phenomenon. In addition, both of them present a high Neel/Curie temperature which makes their properties more stable with respect to temperature fluctuations. In addition modifying deposition the magnetic materials in strips shapes could improve the stability of the magnetization, of the whole stack. The next part presents the main clean room technics involved in the process: lithography and lift-off technic.

2. Main clean room fabrication technics

a) The lithography

This is a basic technic in microfabrication and processes often rely on several lithographic steps. The objective of this method is to protect some part of the wafer and target others a specific step for example an etching of deposition of material. It consists in a spinning a photoresist on the surface of the wafer which is liquid polymer solution sensitive to light. A soft bake allows evaporating the solvent, hardening the resist and improving its adhesion to the wafer. At this step, the face of the wafer is coated by a layer of resist. The wafer is then exposed to a mercury light through a mask and plunge into a developer solution to draw the wanted patterns into the resist. The mask is used to transfer the specific patterns on the photoresist acting like a stencil for the light. Depending on the type of photoresist, positive or negative, the result will be different. In a positive resist, the light breaks the polymer chains and make then more soluble in the developing solution. For a negative photoresist, the light induces a crosslinking of the polymers chains which makes the resist less soluble in the developing solution. In the case of my process, I have been brought to use both types of photoresists.

b) Lift-off Technique

The technique relies on the lithography and has been used to realize the magnetic strips and is presented in the Figure 24. First, it consists, in depositing a very thick layer of resist (>2µm). This latter is exposed to light and developed, revealing the patterns of the mask of the Figure 27. The wafer is then coated by a metal layer. Many different deposition technics may be used: evaporation CVD or PVD. In my case, the wafer is placed inside a RF-PVD chamber to deposit the materials. Finally, the remaining resist and the excess of metal are removed, leaving the magnetic stripes on the wafer. The negative slope of the walls after development of the resist is called undercut and allows the removing solution to easily attack the resist and realize the lift-off.

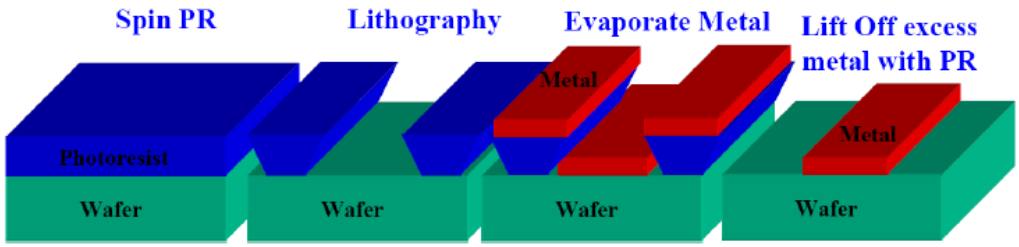

Figure 24: The steps of the lift-off process (extracted from process courses)

In the case of the process studied at the ONERA, the lift off involves four layer composed of two different resists: three layer of LOR, non-photosensitive viscous resist and a top layer constituted by a photosensitive resist. Since only the top layer is photosensitive, the undercut is created during the development of the LOR below the S1813. The size of the undercut depends on the development time. This latter can be easily observed with a microscope. The development time is a critical parameter and determines the size of the undercut. The Figure 25 compares the undercuts obtained after two different development procedures.

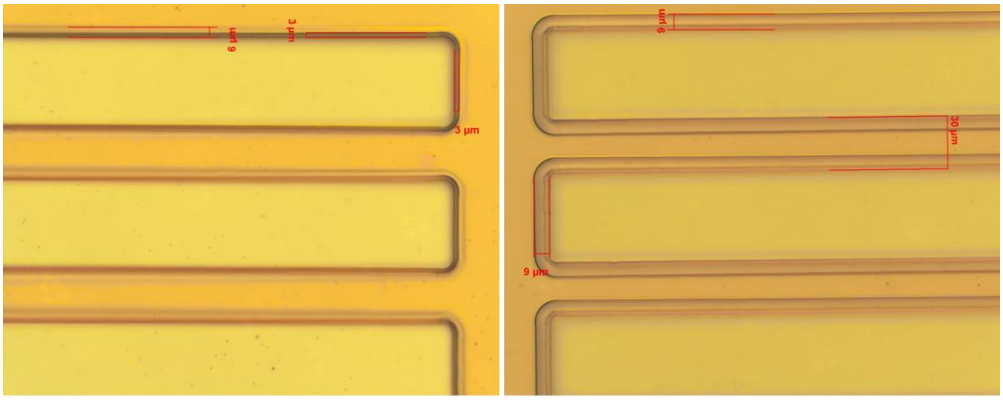

Short development time
undercut = 3µm

Long development time
undercut = 9µm

Figure 25: Square 33 observed with a x50 objective, the development time has a great impact on the size of the undercut.

When the development time is too long and the inter-stripe distance is small (<18µm), it happens that the resist is entirely under etch (see Figure 26(a)).

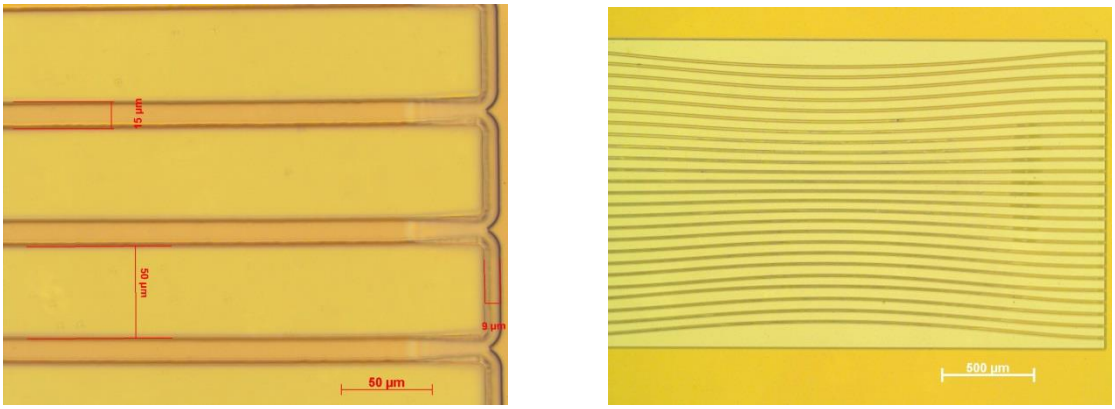

(a) **(b)**

Figure 26: Pattern 36 observed with an optical microscope (a) an overlap of the undercuts is observed. This overlap leads to deformation of the resist (b).

The undercuts overlap below the resist. This weakens the whole structure and most of the time the resist's pattern is distorted (see Figure 26(b)).
Now that the main process technics have been presented, the whole clean room process will be described.

3. Description of the clean room process

The main objective of this process is to deposit stripes of staked magnetic material of different shape to evaluate the impact of the geometry of the stripes on the hysteresis cycle. The concept comes from D. Ettelt [23]who used the same king of features in its device to improve the stability of the magnetic materials. First of all, the process must be optimized to ensure that all magnetic stipes are properly patterned on the wafer. This is the opportunity for me to begin to work in the clean room dedicated to my team and to be trained on the different equipment. Starting from a 3cm² quartz wafer coated on both faces by a gold-chromium layer, the objective is to realize 81 patterns of 3*3mm² playing on the width of stripes and the distance between each of them. The process is composed of 4 lithographic steps including the

numbering of each pattern, the separation of each square and the stripes patterns. The fourth mask is dedicated to test some electrode shapes that occupy the middle line of the wafer. Actually, each stripes pattern is drawn three times on the wafer in case of localized defects on the wafers. This gives in total 24 different patterns to test, on the Figure 27 one can observe the mask used to create those patterns. . The number of stripe is the same on each pattern of each line of square. The three parameters of the patterns are emphasized on the scheme of the Figure 27 among them, the width of the stripes decreases from the top to the bottom (500µm to 2µm). The middle empty squares are used as witnesses.

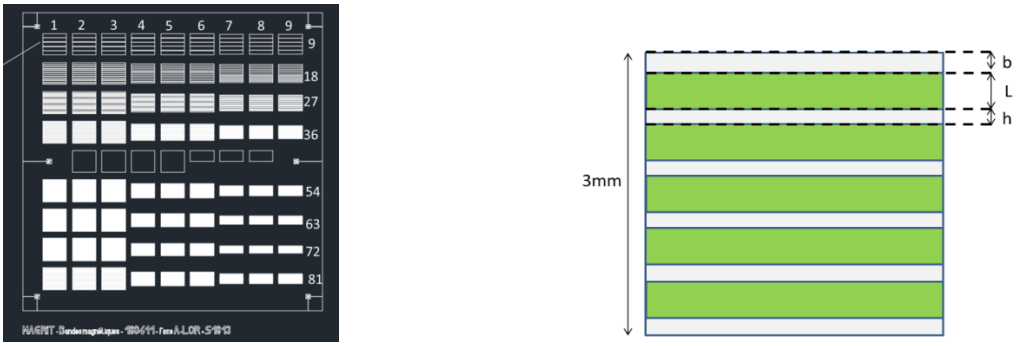

Figure 27: on the left is the mask dedicated to print the stripe patterns; on the right the scheme presents the different parameters that vary from a pattern to another

The Figure 28 described the entire process constituted of nine steps including four lithographies.

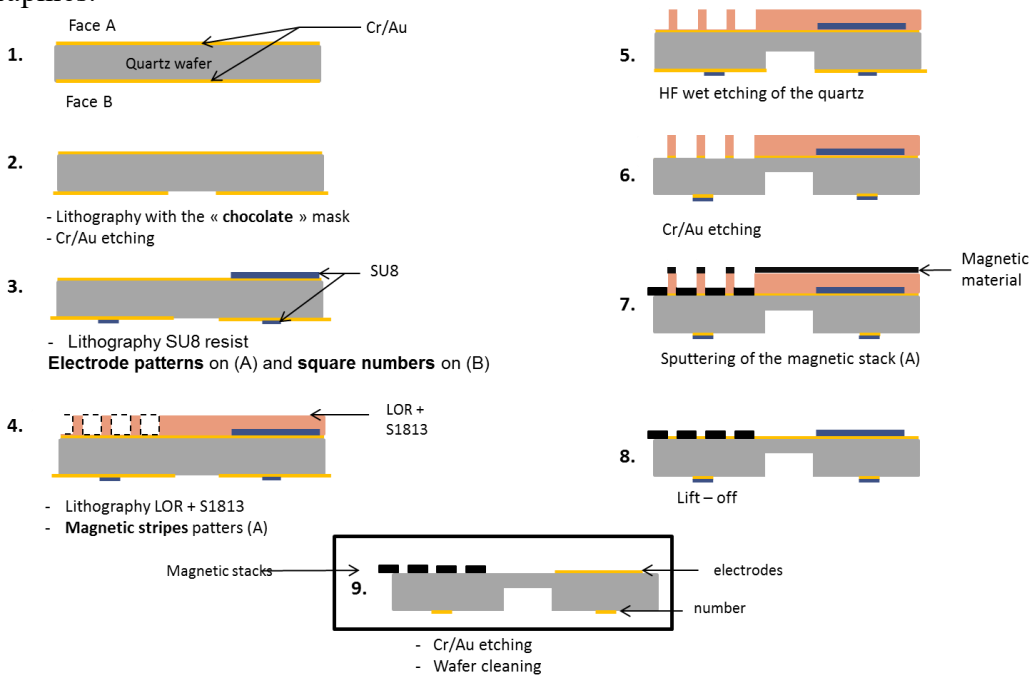

Figure 28: Main steps of the clean room process dedicated to the realization of magnetic material stripe patterns

2. First, the Au/Cr layer is etched to create a grid on the back side of the wafer. This grid will be exploited latter in the process as a mask to etch the wafer in HF/NH_4F solution. This step is quite important because it also creates alignment marks for the next lithographic steps.

3. The SU8 photoresist is then spread on both side of the wafer. The resist is patterned by lithography with the number of the squares on the back side and electrode test shapes on

the front side (see Figure 29). The SU8 is then developed, leaving only the resist exposed to the light on the surface of the wafer.

(a) (b)

Figure 29: Su8 Resist, (a) the number below the square 28, (b) the electrode test patterns on the face A

4. Above the Su8, the resist used to create the stripe patterns is deposited. In reality, this layer is very thick and composed of two different resists: first three layers of LOR and one layer of S1813 that is the only photosensitive layer. The technique used to realize the magnetic strips is the lift-off technique and was presented in the previous section.
5. Then, the back side of the wafer must be etched during 28h with hydrogen florid (HF) to create a grid pattern that will allow separating the 81 little squares at the end (see Figure 30).

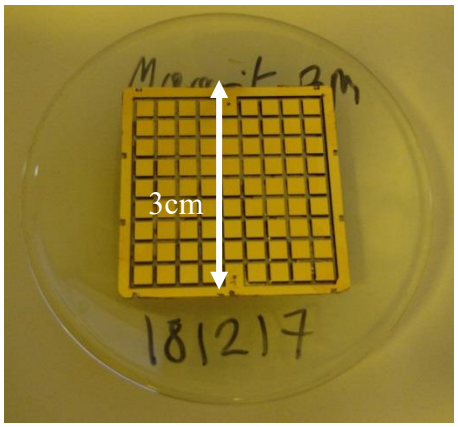

Figure 30: Back side of the wafer after the etching step

Since the Au/Cr coating is resistant to HF, it acts as a mask to pattern the grid. To evaluate the resistance of the deposited resists to this long HF etching step, I performed some characterization analysis using a microscope and a profilometer. Observations have been carried before and after the etching step.
The Figure 31 emphasizes that the etching step did not altered the resist patterns. Indeed the striped shapes are well conserved during this procedure.

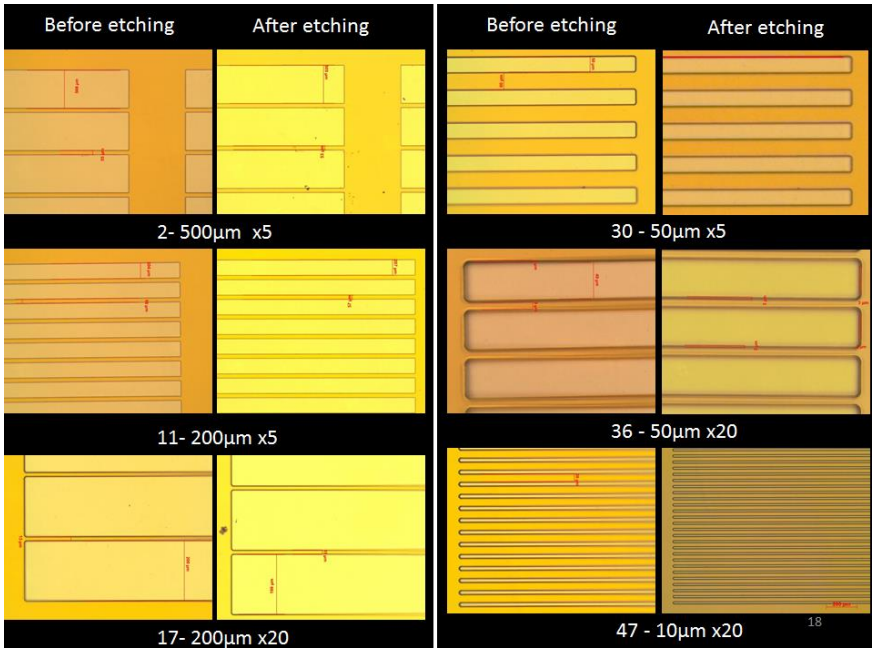

Figure 31: Comparison between some stripe patterns before and after the etching step observed through a microscope with different optics. The number corresponds to first the number of the square then the width of the stripe and the magnification.

The profilometer allows recording a resist thickness of 5µm constant all over the wafer. The Figure 32 presents the measurement at the edge of a test square.

(a)

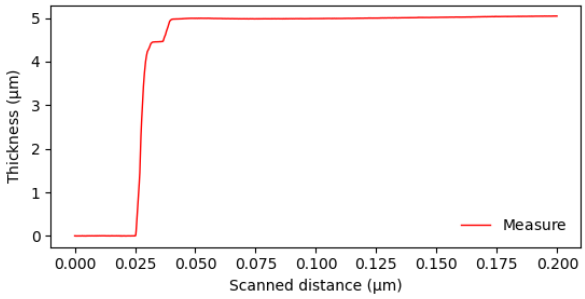

(b)

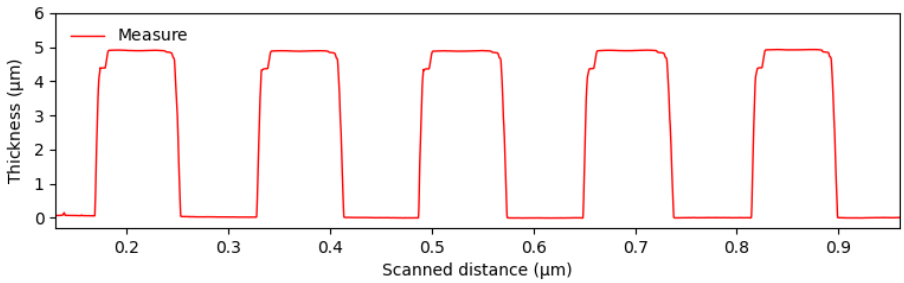

Figure 32: Measurement of the resist thickness by profilometry at the edge of one pattern (a) and through 1mm of a 100µm-stripe pattern (b)

6. The next step consists in removing the Au/Cr layer where the magnetic stack is going to be deposited. This step was particularly difficult because only a random number of stripes were correctly etched. I detail the issue in a next section. When a stripe is correctly etched,

it is possible to observe the undercut and the slight underetch of the golden layer the Figure 33 illustrates this phenomenon:

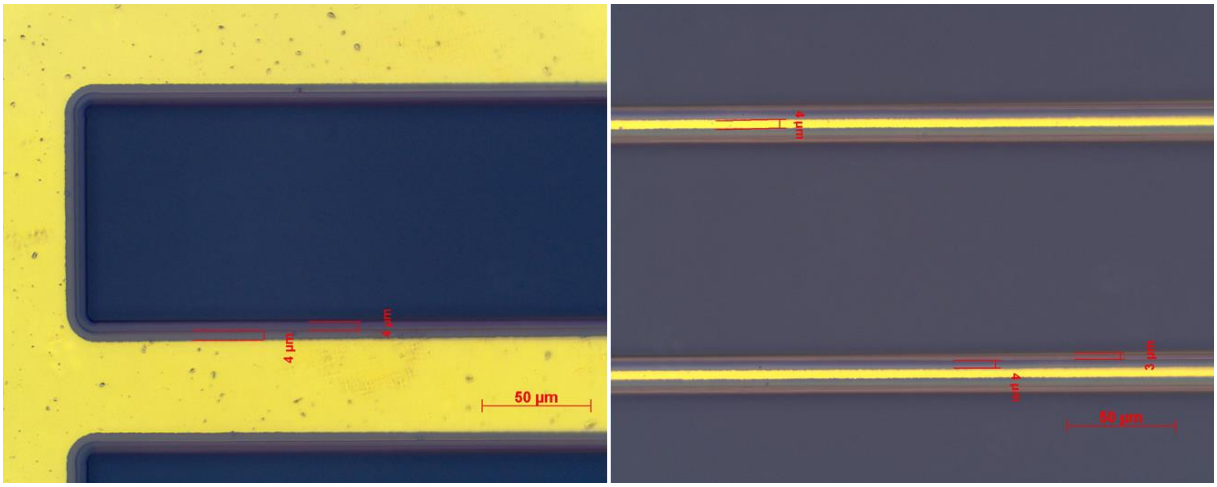

Figure 33: Undecut (3-4µm) and undertch (4µm) on 100µm large stripes

7. If the stripes are correctly etched, the magnetic materials are deposited by means of RF PVD (see Appendices p47). Two different stacks have been experimented: one with a first 20nm layer of NiCr and acting as an adhesive layer between the substrate and the stack. Then, the two main magnetic materials are alternatively sputtered on the whole wafer to create a stack: $[NiMn/FeCo]_{10}/NiMn$. Each layer is 50nm thick. The last NiMn deposition allows protecting the whole stack from corrosion. The other tested option involves Tantalum replacing the 20mn of NiCr but also covering the whole stack. These choices are discussed in the last section of the report.
8. After the deposition of the magnetic stack, the lift off takes place, removing all the excess of metal. The only resist remaining on the surface of the wafer is the SU8 that patterns the electrodes.

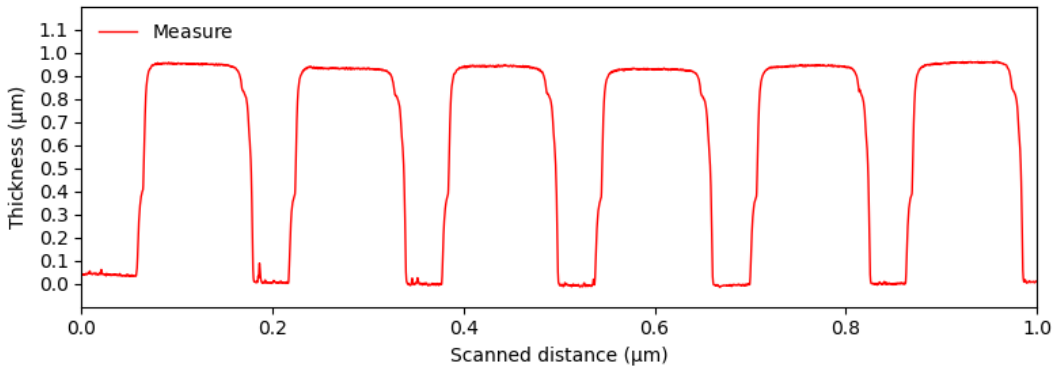

Figure 34: Metal stack with Tantalum after lift off on 100µm-large stripe pattern

The Figure 34 presents the profile of one of the pattern after lift off covered by 50nm of Tantalum. The height of the stack is around 920nm to which must be added the thickness of the chromium/gold layer - 200nm - that is still present everywhere but below the metals. This gives a total thickness of 1120nm which corresponds to the expected quantity of metal.

9. At this moment the remaining gold/chromium on the wafer is supposed to be etched. However, the first time I completed this process, I discovered that those chemicals also attack the deposited stack cleaning the entire wafer

During my next attempts, I stopped the process just after the lift off. In order to avoid this problem and complete the entire process, it has been proposed by my supervisor to sputter Tantalum to protect the whole stack from the etchants. This modification of the process is detailed in the next section with other evolutions.

4. Evolution of the process

The clean room process has been modified several times during the experiment. However, it must be kept in mind that the order of the different steps described previously must not be changed since this process must be compatible with the fabrication of the resonator.

a) Resist adhesion

It appears quite soon that one of the main issues of the process was the weak adhesion of the different resists onto the wafer. This was particularly striking with the resists involved in the electrodes (Figure 35) or the backside numbering but also with the resist involved in the lift off.

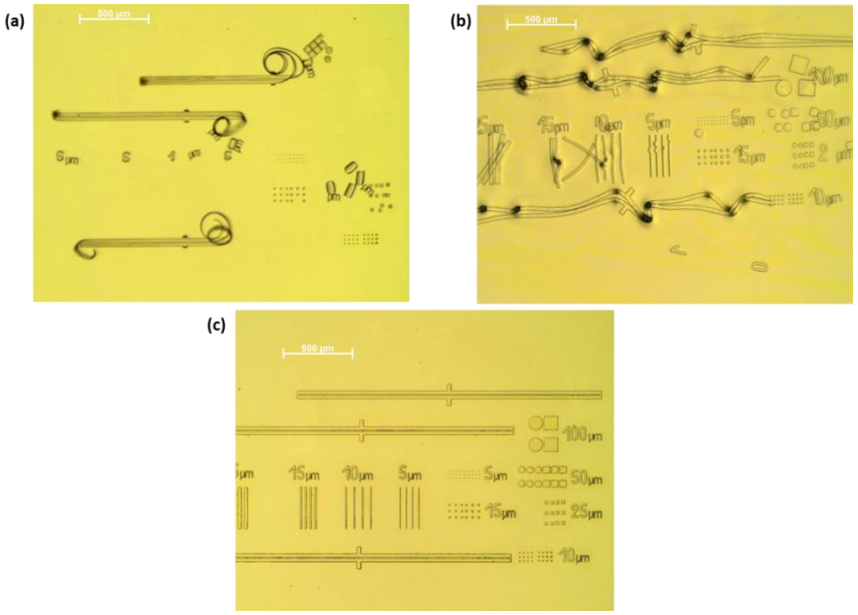

Figure 35: (a) SU8 resist after development, (b) the same resist after spinning of the LOR above and (c) after correction of the process the resist of the electrode stick to the wafer even after the LOR spinning

Concerning the electrode patterns presented in the Figure 35(a), the issue came from the fact that the resist was not sticking on the wafer after the development. To overcome this issue it has been proposed to do a thermal annealing before the spin coating of the SU8 to eliminate the remaining molecule of water or impurities present on the surface. Even if this new step allowed a correct pattern after the development to be obtained, spinning the LOR resist over the SU8 was enough to alter the resist shape again as shown in Figure 35 (b). To consolidate the Su8, several drying steps have been added along the development and in particular a 5min hard bake to conclude this part of the process. All those modifications allowed to obtain the patterns presented in Figure 35(c).

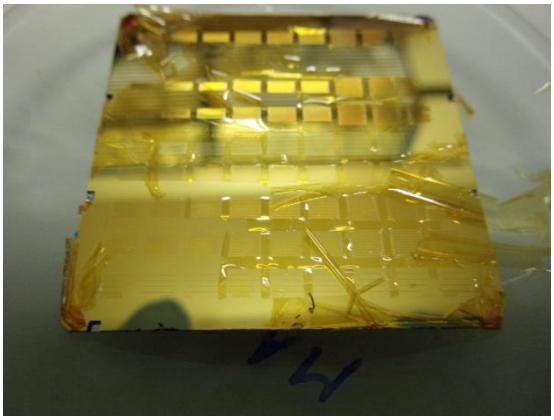

Figure 36: Lift off resist after drying

In the Figure 36 it is possible to observe the resist that completely torn apart. The hypothesis was the presence of a thin film of water on the surface of the wafer that appears when exposed to the clean room atmosphere during a long time. This film heavily affects the sticking properties of the resist to the surface of the wafer. Under the advice of the clean room technicians, a thermal annealing was added right before the spinning of the LOR resist correcting the problem.

b) Tantalum sputtering

As previously said, the last step consists in etching the remaining Au/Cr to reveal the electrode test patterns. The Figure 37 is a picture of my first realization: the entire wafer has been cleaned by the last step of the process.

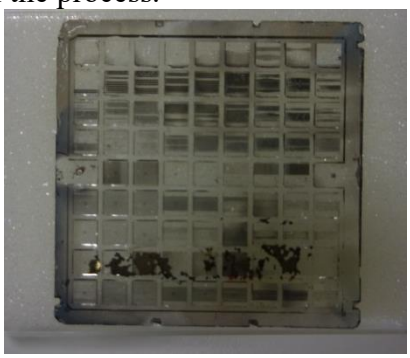

Figure 37: The first wafer I processed has been entirely cleaned by the last step of the process

The shades of grey that can be observed are just few traces of metal still attached to the wafer. In the next realization I stop the process just before the etching step. However, some changes occurred on deposited stack of magnetic materials on another processed wafer after a month. With the optical microscope it is now possible to observe artefacts all over the stripes, in particular near the edges that were absent jut after the lift off. This evolution was quite surprising and it has been decided to observe one of the defects with SEM. The SEM present at the ONERA is equipped with an Energy Dispersive Spectroscopy (EDS) apparatus which allows to analyze the chemical composition near the surface.

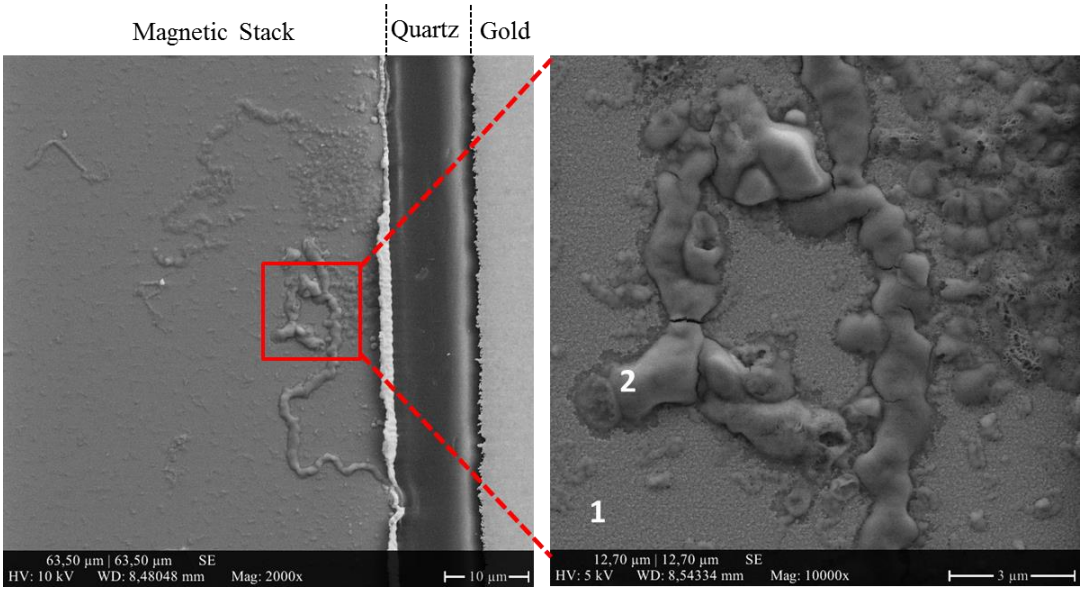

Figure 38: SEM images of a defect at the edge of a stripe

EDS has been performed on the points 1 and 2 of the Figure 38 respectively corresponding to a clean surface and to a damaged surface. Considering the EDS analysis presented in Figure 39, two peaks appears corresponding chromium and oxygen. These signals confirm that these defects are due to the oxidation of the Chromium present in the adhesive layer. It can also be noticed that some chlorine is detect were the stack is attacked.

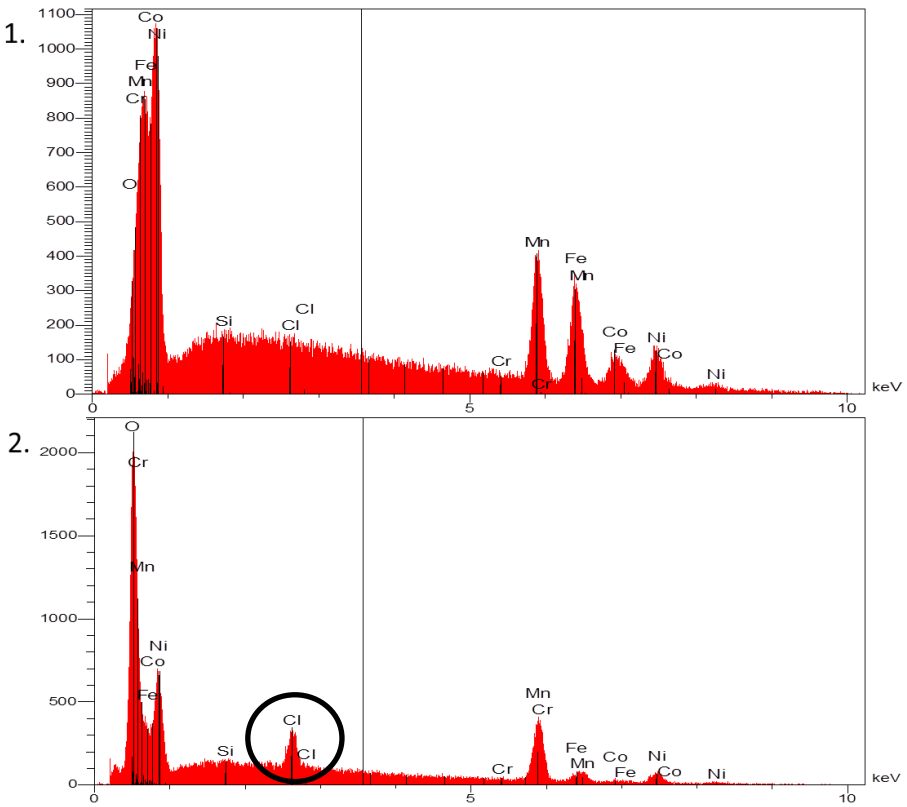

Figure 39: EDS signals captured on an healthy area (1) and on a damage part of the surface where chromium oxide and chlorine are detected (2). These numbers corresponds to the one of the figure 36.

After investigation, it appears that chlorine is present in the solution used to etch the chromium/gold layer. Moreover, the step before the deposition of the metals involves these

etchant solutions. It means that he adhesion layer may have been attacked by a remaining traces of etching solution.
It has been proposed to encapsulate the magnetic stack between two layers of Tantalum. Since it is possible to use simultaneously three targets inside the sputtering machine, this material would be deposited in a row with the NiMn and FeCo. The Tantalum is a non-magnetic metal and is highly resistive to corrosion what makes it a promising candidate to protect our magnetic materials. Tantalum could replace the NiCr adhesion layer to avoid any contamination from the bottom of the stack. In addition, the lattice structure of the Tantalum (a=3.30 Å) is further from the one of the antiferromagnetic phase of the NiMn than NiCr alloy. Indeed, during its studies of the magnetic materials, my tutor observed a drop of the exchange bias for layer near the substrate. He noticed that the NiCr has a cubic face centered structure (a=3.55Å) close to the γ-phase of the NiMn. This would prevent the transition of the NiMn to its antiferromagnetic phase by local epitaxy phenomenon [24].
The structure of the stack has been modified to encapsulate the magnetic materials between two Tantalum layers. This gives: Ta/[NiMn/FeCo]$_{10}$/NiMn/Ta all the layers are 50nm thick except the first layer of Tantalum of 20nm replacing the NiCr film. The Figure 40 presents the evolution of the stack.

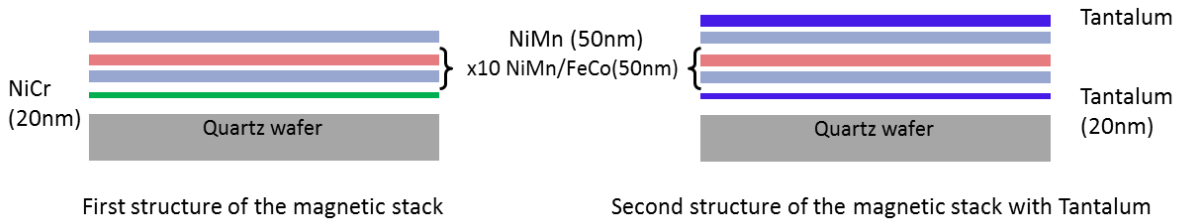

Figure 40: Evolution of the structure of the sputtered magnetic stack

During the first tests of resistance to gold etchants, it appears that even the tiniest defect into the Tantalum layer induces a deterioration of the stack (see Figure 42). However, when focusing on preserved part of a stripe it was possible to observe correct profile of the stack like the one of the Figure 41.

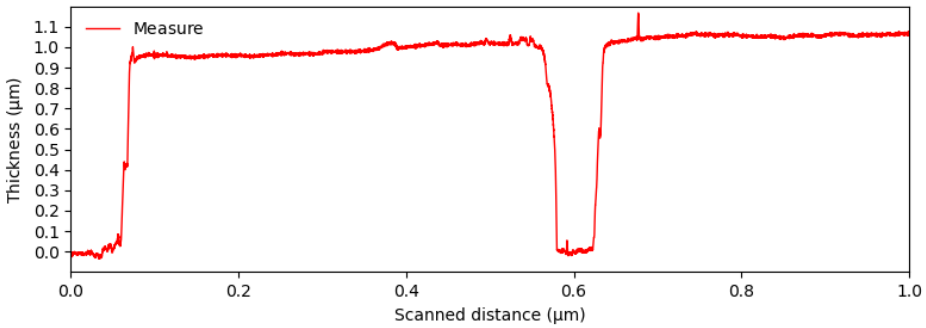

Figure 41: Profile of the stack after etching the surrounding gold layer over 1mm

To study the influence of Tantalum in the stack as protection layer against etchant, it has been chosen to sputter different thickness of Tantalum: from 50nm up to 200nm.

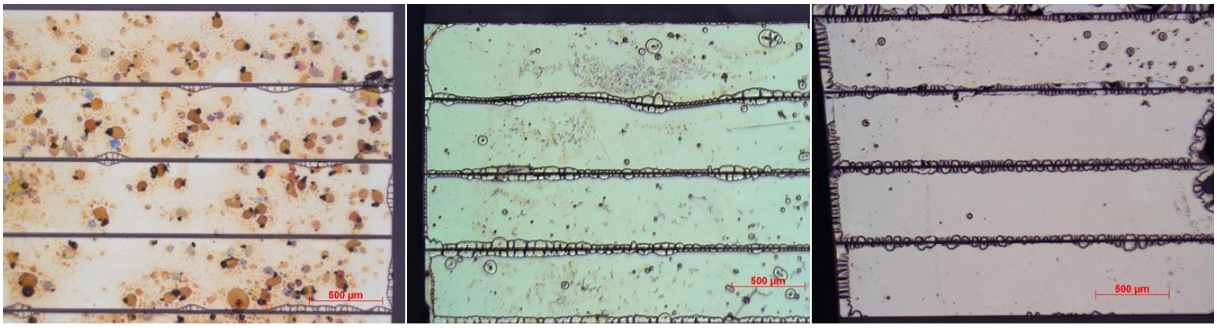

Figure 42: Impact of the gold etchants on the magnetic stacks for different thickness of Tantalum

In the Figure 42 it is possible to see that the Tantalum is not directly attacked by the etchants. The different traces correspond to local oxidation of the magnetic material below the Tantalum layer, indeed the etchants penetrate through defects in the protection film. It can also be noticed that the surface state gets better as the thickness of the layer of Tantalum increases. The next step would consist in improving the homogeneity of the deposition of the Tantalum layer to avoid the remaining defects. First, tilting the sample during the sputtering process could offer a better conformity of the layer, in particular on the edge of the stack, where the tantalum does not totally wrap up the stack leading to underetch (see Figure 43).

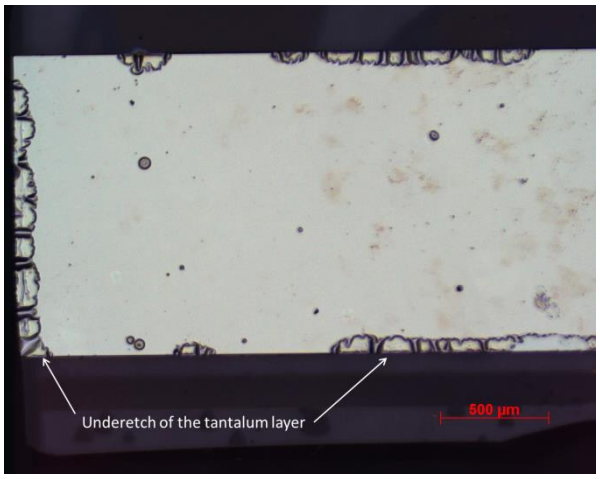

Figure 43: Underetch of the tantalum layer are visible on the edges of most of the stacks

A second option would consist in changing of deposition process of the last layer, using e-beam evaporation instead of RF sputtering. The evaporation is the process used to deposit the chromium/gold layer present on the wafer and allows tight thin films to be realized. Even if the melting temperature of the Tantalum being quite high (3000°C) the e-beam evaporation is feasible but will require a long period of test to find the best deposition parameters
Finally, these results are quite positive and several options in the use of the Tantalum remain to explore. In addition, the target of Tantalum took several weeks to arrive at the ONERA and it was too late to realize magnetic analysis of the different patterns. To conclude, the whole process has evolved a lot during this internship and became almost viable for the realization of magnetic stripes in between 500µm down to 10µm larges.

Conclusion and future outlook

The master thesis project realized at the ONERA allowed a better understanding of the conception of quartz based MEMS and more particularly a MEMS magnetometer. It has been possible to evaluate the performances of the devices under development involving different characterization technics: electrical characterization, optical vibrometry, Raman spectroscopy for surface quality verification. All of this allowed to investigate on the ways to approach the values of quality factor predicted by a model established with a simulation software. It has been found that the thermal annealing of a quartz resonator improves significantly its quality factor due to crystalline rearrangement of the electrodes. Despite the failure of one of the equipment, the impact of the gold electrodes remains to be studied in-depth.
These twenty two week were also, for me, the opportunity to work on the optimization of a clean room process: the realization magnetic material stacks pattern in stripes shapes. In total nine wafer were involve in the study, after each step each of them was carefully observed with microscope and profilometer. The objective was to obtain as much as possible exploitable pattern at the end of the process.
Concerning the future work, the quality factor of the torsional resonator can still be improved to fill the gap with the theoretical model. In particular it will be interesting to investigate the influence of the gold electrodes on the resonator performances. On the side of the magnetic stripes study, the permeability to the etchants must be improved and the different patterns realized should be tested to emphasize the magnetic behavior according to the geometry of the stripes.

Finally, this project was very enriching concerning the knowledge I acquired; gathering the elaboration and development of a quartz MEMS but also the technic with the different equipment that I have been using. It was also for me the opportunity from a social point of view to participate to the life of the CMT team at the ONERA: meetings and events such as the days dedicated to the Inertial MEMS. This was the fifth Inertial Days (Journées micro et nano technologies pour l'inertiel) taking place the 26-27th of March in the ONERA's facilities at Palaiseau. During these two days several French companies met to realize a State of the Art of the nano and micro technology dedicated to the inertial measurements.

References

[1] J. Lenz and A. S. Edelstein, “Magnetic sensors and their applications,” *IEEE Sens. J.*, vol. 6, no. 3, pp. 631–649, 2006.

[2] “fr @ www.onera.fr.” [Online]. Available: https://www.onera.fr/fr.

[3] “dphy @ www.onera.fr.” .

[4] Y. Matsumoto, S. Kawahito, Y. Tadokoro, S. O. Choi, and M. Ishida, “An integrated micro fluxgate magnetic sensor,” *Sensors Actuators A Phys.*, vol. 55, no. 2–3, pp. 121–126, 2002.

[5] R. S. Popovic, *Hall Effect Devices*, Taylor & F. Lausanne: Institute of Physics Publishing Bristol and Philadelphia, 2003.

[6] A. Guedes *et al.*, “Towards picotesla magnetic field detection using a GMR-MEMS hybrid device,” *IEEE Trans. Magn.*, vol. 48, no. 11, pp. 4115–4118, 2012.

[7] M. H. Phan and H. X. Peng, “Giant magnetoimpedance materials: Fundamentals and applications,” *Prog. Mater. Sci.*, vol. 53, no. 2, pp. 323–420, 2008.

[8] A. Dankert, B. Karpiak, and S. P. Dash, “Hall sensors batch-fabricated on all-CVD h-BN/graphene/h-BN heterostructures,” *Sci. Rep.*, vol. 7, no. 1, pp. 1–7, 2017.

[9] F. Kobbi *et al.*, “High sensitivity hall sensors with low thermal drift using AlGaAs/InGaAs/GaAs heterostructures,” *Sensors Actuators A Phys.*, vol. 43, no. 1–3, pp. 135–140, 2002.

[10] N. Behbood, F. Martin Ciurana, G. Colangelo, M. Napolitano, M. W. Mitchell, and R. J. Sewell, “Real-time vector field tracking with a cold-atom magnetometer,” *Appl. Phys. Lett.*, vol. 102, no. 17, 2013.

[11] D. A. Buttry and M. D. Ward, “Measurement of Interfaclal Processes at Electrode Surfaces with the Electrochemical Quartz Crystal Microbalance,” *Chem. Rev.*, vol. 92, no. 6, pp. 1355–1379, 1992.

[12] C. Zener, “Internal Friction in Solids II. General Theory of Thermoelastic Internal Friction,” *Phys. Rev.*, vol. 53, no. 1, pp. 90–99, Jan. 1938.

[13] R. Lifshitz and M. L. Roukes, “Thermoelastic damping in micro- and nanomechanical systems,” *Phys. Rev. B*, vol. 61, no. 8, pp. 5600–5609, Feb. 2000.

[14] R. Levy, T. Perrier, P. Kayser, B. Bourgeteau, and J. Moulin, “A micro-resonator based magnetometer,” *Microsyst. Technol.*, vol. 23, no. 9, pp. 3937–3943, 2017.

[15] T. Perrier, R. Levy, P. Kayser, B. Verlhac, and J. Moulin, “Modeling of a vibrating MEMS magnetometer partially covered with a ferromagnetic thin film,” in *2018 IEEE International Symposium on Inertial Sensors and Systems (INERTIAL)*, 2018, pp. 1–4.

[16] R. Levy and V. Gaudineau, “Phase noise analysis and performance of the Vibrating Beam Accelerometer,” *2010 IEEE Int. Freq. Control Symp. FCS 2010*, pp. 511–514, 2010.

[17] L. J. Slutsky and W. H. Wade, “Adsorption of Gases on Quartz Single Crystals,” *J. Chem. Phys.*, vol. 36, no. 10, pp. 2688–2692, May 1962.

[18] C. Barker and B. E. Torkelson, “Gas adsorption on crushed quartz and basalt,” *Geochim. Cosmochim. Acta*, vol. 39, no. 2, pp. 212–218, Feb. 1975.

[19] “spectrum @ www.ens-lyon.fr.” [Online]. Available: http://www.ens-lyon.fr/LST/Raman/spectrum.php?nom=quartz (powder).

[20] J. Nogues and I. K. Schuller, “0827.J.Magn.Magn.Mater.1999,192,203.pdf,” *J. Mag. Mag. Mater.*, vol. 192, pp. 203–232, 1999.

[21] W. H. Meiklejohn, “Exchange Anisotropy—A Review,” *J. Appl. Phys.*, vol. 33, no. 3, pp.

1328–1335, Mar. 1962.
[22] J. P. Nozières, S. Jaren, Y. B. Zhang, A. Zeltser, K. Pentek, and V. S. Speriosu, “Blocking temperature distribution and long-term stability of spin-valve structures with Mn-based antiferromagnets,” *J. Appl. Phys.*, vol. 87, no. 8, pp. 3920–3925, 2000.
[23] D. Ettelt, P. Rey, G. Jourdan, A. Walther, P. Robert, and J. Delamare, “3D magnetic field sensor concept for use in inertial measurement units (IMUs),” *J. Microelectromechanical Syst.*, vol. 23, no. 2, pp. 324–333, 2014.
[24] B. Y. Wong, C. Mitsumata, S. Prakash, D. E. Laughlin, and T. Kobayashi, “The interplay between NiMn/NiFe epitaxial growth and NiMn atomic ordering in NiMn/NiFe exchange biased layers: a structural perspective,” *IEEE Trans. Magn.*, vol. 32, no. 5, pp. 3425–3427, 1996.

Appendices

A- RF Sputtering PVD

The Physical vapor deposition (PVD) gathers all technics of deposition of thin film by means of condensation of a vapor onto a cooler substrate. This wide concept can be divided in two categories: evaporation and sputtering. To realize the deposition of magnetic material I have used RF sputtering (Figure 44).

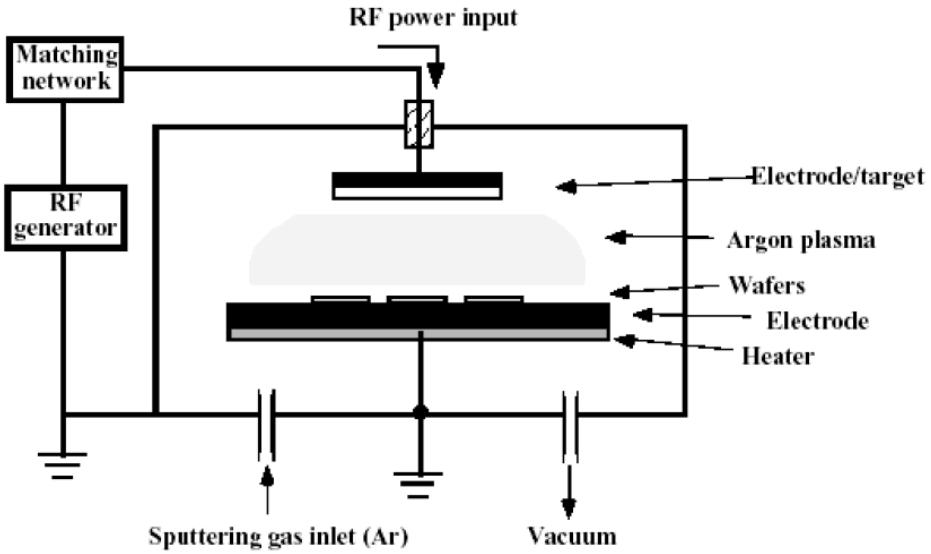

Figure 44 : RF Sputtering PVD (extracted from courses)

The substrate is placed in a vacuum chamber on an electrode. A target composed of the material to deposit is place above and constitutes the second electrode. An Argon plasma is generated between the electrodes and sputtering occurs on the target. The sputtered atoms travel through the plasma and deposit on the wafer. During the whole operation the target and the substrate are cooled by water so that the temperature is kept quite low in comparison with other deposition method. For example, in the evaporation technique, the material to be deposited is annealed at high temperature: 1200-1800°C.
With the apparatus used at the ONERA it is possible to load up to three targets and to change them without breaking the vacuum of the chamber which is quite interesting since the magnetic stack is composed of a tenth of layers. The Figure 45 presents the machine used at the research lab.

Closed Open

Figure 45: PVD apparatus, when the machine is opened, it is possible to change the targets in the top part and load the substrates in the chamber bellow

This machine is quite large and can process very large substrates as witnesses the Figure 46.

Figure 46: On the left, this is the Iron Cobalt target and on the right on can see two of my wafer 3cm large each ready to be processed

B- Gantt Diagram (retrospective)

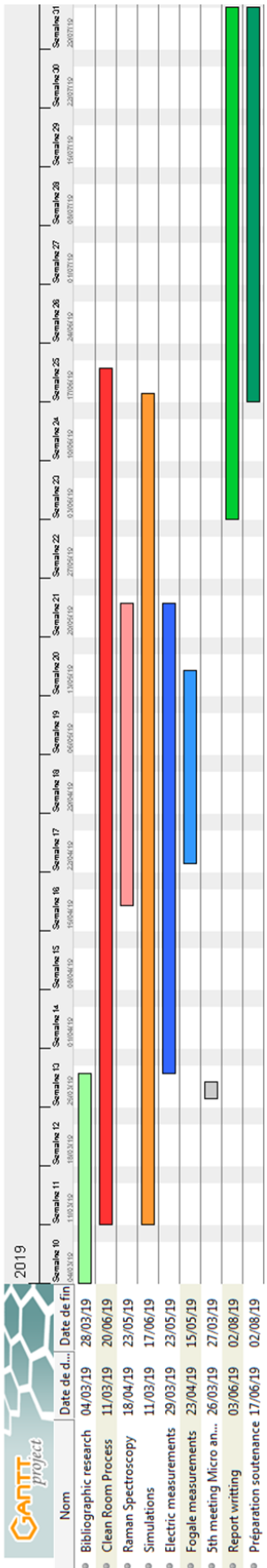

(realized with the Ganttproject software)

Task	Starting date	Ending date
Bibliographic research	04/03/19	28/03/19
Clean Room Process	11/03/19	26/06/19
process1 11/03 - 22/03 *process2 02/04 - 05/04 wafer cassé* *process3 09/04 - 19/04* *process4/5 06/05 - 16/05* *process6/7 27/05 - 06/06* *process8 08/06 - 09/06*		
Raman Spectroscopy	18/04/19	23/05/19
Simulations	11/03/19	17/06/19
Electric measurements	29/03/19	23/05/19
Fogale measurements	23/04/19	15/05/19
Journée de l'inertiel	26/03/19	27/03/19
Report writting	03/06/19	02/08/19
Defense groundwork	17/06/19	02/08/19

C- Detail of the calculation of the value of α to find H_{Ex}

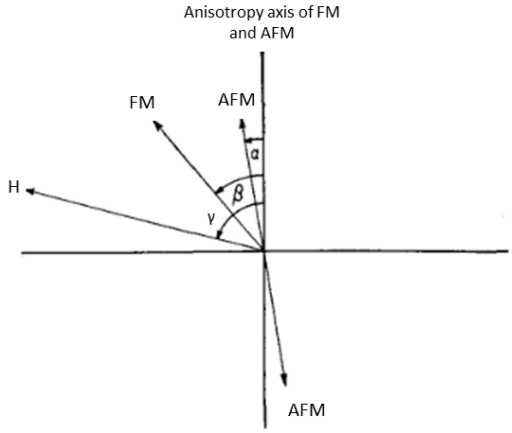

Figure 47: Vector diagram identifying the different angles (adapted from [21]**)**

From the equation (12) the system below can be established

$$\begin{cases} \dfrac{J_{Ex}}{K_{AFM}t_{AFM}} = \dfrac{\sin 2\alpha}{\sin(\beta-\alpha)} & \textit{Derivation with respect to } \alpha \\ \dfrac{J_{Ex}}{HM_{FM}t_{FM}} = \dfrac{\sin(\gamma-\beta)}{\sin(\beta-\alpha)} & \textit{Derivation with respect to } \beta \end{cases}$$

Considering the case where $K_{AFM}.t_{AFM} >> J_{Ex}$, one can write the following inequality:

$$\frac{J_{Ex}}{K_{AFM}t_{AFM}} \geq \frac{\sin 2\alpha}{\sin(\beta-\alpha)} \geq \sin 2\alpha$$

$$\alpha \leq \frac{1}{2}\arcsin\left(\frac{J_{Ex}}{K_{AFM}t_{AFM}}\right) \qquad (16)$$

We have: $\frac{J_{Ex}}{K_{AFM}t_{AFM}} \to 0$ then, $\frac{1}{2}\arcsin\left(\frac{J_{Ex}}{K_{AFM}t_{AFM}}\right) \to 0$
Since the right term of the equation (16) tend towards 0, α tends towards 0.

D- Lorentzian model

Considering the mechanical model of a quartz resonator, the movement equation is

$$\ddot{x} + \frac{\omega_0}{Q}\dot{x} + \omega_0^2 x = F/M$$

This can be rewritten

$$(\mathrm{j}\omega)^2\mathrm{x} + \frac{\omega_0}{Q} j\omega x + \omega_0^2 x = F/M$$

The displacement can be expressed:

$$x = \frac{F/M}{-\omega^2 + \frac{\omega_0}{Q} j\omega + \omega_0^2}$$

We set $\delta\omega = \omega - \omega_0$, then replacing gives:

$$x = \frac{F/M}{-2\delta\omega\omega_0 + \delta\omega^2 + \frac{\omega_0^2}{Q} j + j\frac{\omega_0 \delta\omega}{Q}}$$

We consider that we are near the resonance: $\delta\omega/\omega_0 \ll 1$, then

$$x = \frac{F/M}{-2\delta\omega\omega_0 + \frac{\omega_0^2}{Q} j}$$

Thus writing the square modulus of the displacement, we obtain:

$$|x|^2 = \frac{\left(\frac{F}{2M\omega_0}\right)^2}{\delta\omega^2 + \left(\frac{\omega_0}{2Q}\right)^2}$$

We set $\mathrm{X}_{max} = \frac{FQ}{M\omega_0^2}$

Finally, the square root of the modulus of the displacement can be written under the form of a Lorentzian function:

$$|x|^2 = \frac{{X_{max}}^2 \left(\frac{\omega_0}{2Q}\right)^2}{\delta\omega^2 + \left(\frac{\omega_0}{2Q}\right)^2}$$

Abstract

This report sums up my master thesis project that took place at the ONERA in Chatillon. During these twenty two weeks, I joined the team CMT specialized in the design of inertial MEMS for aerospace applications including the elaboration up to the integration with on board electronics. My team's research is based on direct need of the industry or personal initiative of the team members. Initially the work was based on quartz accelerometer and gyrometers. Nevertheless, the research field tends to broaden, first with the realization of magnetometers and time reference resonator based on quartz but also with the recent subjects involving promising materials such as graphene based gas sensor or gyrometer in GaAs.
My work hinged on the research my tutor carried during his PhD: the design and realization of MEMS magnetometer. First of all, I have been involved in the characterization of the resonators dedicated to the fabrication of the magnetometers. This work consisted in electric and optical characterizations of the devices to evaluate their performance and determine their figure of merit: quality factor and resonance frequency. Therefore, I participated to the development and improvement to a clean room process dedicated to study the impact of the shapes of the deposited magnetic materials. This part consisted in a self-sufficient work in clean room but also periodic meeting to present the different results or issues encountered during the process.

Résumé

Ce rapport présente les travaux que j'ai réalisés au cours de mon Projet de Fin d'étude à l'ONERA au sein du site de Chatillon. Au cours de ces vingt-deux semaines, j'ai intégré l'équipe CMT (Capteurs et Micro Technologies) spécialisée dans les capteurs MEMS dédiés à l'inertiel. Leur travail comprend le design de capteurs jusqu'à leur intégration avec un system électronique embarqué de type FPGA. L'équipe CMT se concentrait à l'origine sur le développement de gyromètres et d'accéléromètres mais a progressivement élargi son domaine d'expertise et s'occupe plus récemment du développement d'un magnétomètre et d'un résonateur dédié aux références temps et fréquences. Même si la majorité des MEMS étudiés dans mon équipe sont réalisés à partir de wafer de quartz CMT s'intéresse aussi à des matériaux prometteurs comme le graphène pour l'élaboration de détecteur de gaz ou encore le Arséniure de Gallium pour la réalisation de gyromètres.
Mon stage s'est articulé autour des travaux réalisés par mon maître de stage pendant sa thèse axée sur le développement d'un magnétomètre. J'ai d'abord été amené à caractériser électriquement et optiquement différents résonateurs en vue de leur utilisation en tant que magnétomètres, mon but étant d'extraire leur fréquence de résonnance et leur facteur de qualité. Dans un second temps, j'ai participé au développement d'un procédé salle blanche dédié à la réalisation de bandes de matériaux magnétiques de différentes tailles. Pour ce faire j'étais amené à travailler de façon autonome en salle blanche mais aussi à consulter mes collègues pour présenter mes résultats ou en cas de problème.

Abstract

Questo rapporto riassume il mio progetto di tesi di laurea che ha avuto luogo presso l'ONERA di Chatillon. Durante queste ventidue settimane, sono entrato a far parte del team CMT specializzato nella progettazione di MEMS inerziali per applicazioni aerospaziali compresa l'elaborazione fino all'integrazione con l'elettronica di bordo. La ricerca del mio team si basa sulla necessità diretta dell'industria o sull'iniziativa personale dei membri del team. Inizialmente il lavoro era basato su accelerometri e girometri al quarzo, ma il campo tende ad allargarsi, prima con la realizzazione di magnetometri e risuonatori di riferimento temporale basati sul quarzo ma anche con i recenti soggetti che coinvolgono materiali promettenti come il sensore di gas basato sul grafene o il giroscopio in GaAs.
Il mio lavoro dipendeva dalla ricerca svolta dal mio tutor durante il suo dottorato: la progettazione e la realizzazione del magnetometro MEMS. Innanzitutto, sono stato coinvolto nella caratterizzazione dei risonatori dedicati alla fabbricazione dei magnetometri. Questo lavoro consisteva in caratterizzazioni elettriche e ottiche dei dispositivi per valutare le loro prestazioni e determinare la loro cifra di merito: fattore di qualità e frequenza di risonanza. Quindi, partecipo allo sviluppo e al miglioramento di un processo di stanza pulita dedicato allo studio dell'impatto delle forme dei materiali magnetici depositati. Questa parte consisteva in un lavoro autosufficiente in camera bianca, ma anche riunioni periodiche per presentare i diversi risultati o problemi incontrati durante il processo.